An urban drainage scheme for large-scale flood models

Augusto Getirana*[1,2], Felipe Mandarino[3], Patricia Ney de Montezuma[4], Dalia Kirschbaum[1]

[1]Hydrological Sciences Laboratory, NASA Goddard Space Flight Center, Greenbelt, MD, United States
[2] Science Applications International Corporation, Greenbelt, MD, USA
[3]Instituto Pereira Passos, Rio de Janeiro, Brazil
[4] Rio Aguas, Rio de Janeiro, Brazil

Abstract:

As flood modeling spatial resolutions get finer, physical processes normally neglected, such as urban drainage, must be accounted for. Here, we describe and evaluate an urban drainage scheme for large-scale flood models. The parameterization accounts for urban imperviousness, and water flow over streets and through a prescribed urban drainage network. A parameter sensitivity analysis is performed during three major extreme floods over Rio de Janeiro city, Brazil, at ~200m spatial resolution. Results show that, compared to a hypothetical case without urban drainage, representing a drainage network decreases urban flooding during selected extreme events across Rio de Janeiro by 31-53%. Such a decrease is caused by an underground water storage of up to 2.5 billion m^3 across the city during flood peaks. Underground water storage and transport smooth out and delay peak flows by a few hours over major rivers and channels draining the city. Simulations also indicate that the number of residents exposed to flooding drops by 60-80%, from ~5 million to 1-2 million, when an urban drainage system is considered during extreme events. Similar proportions are found for social infrastructure (i.e., schools and hospitals) exposed to flooding. Results reveal that racial minority and low-income populations could disproportionally be exposed to extreme floodings across the city. We conclude that representing urban drainage has a substantial impact on flood exposure and should be accounted for in fine resolution modeling. The proposed scheme is particularly useful in poorly monitored cities and where extreme floods are a frequent hazard yet to be tackled.

Plain Language Summary:

This paper describes an original development that addresses issues related to flood modeling at fine resolutions. In the framework of a project developed between NASA and the municipality of Rio de Janeiro, we have been developing a flood monitoring system at the city scale (~200-meter resolution). Our approach is based on the HyMAP global flood model, and adapt it to represent urban drainage. The parameterization of the proposed urban drainage module accounts for urban imperviousness, and water flow over streets and through a prescribed urban drainage network. HyMAP is coupled with the Noah-MP land surface model within the NASA Land Information System (LIS). This holistic approach represents floods from both rainfall and channel overflow, by integrating vertical water and energy balance processes, surface water dynamics over rivers, channels, urban areas, and interactions with an underground drainage system. Based on model experiments considering different parameterizations, municipal data and demographic surveys, we analyze population and social infrastructure exposure to flooding. Population data is further decomposed based on income, race and ethnicity. Also, another goal of this paper is to document the data requirements and processing steps that can be used as a guideline for further replication in other regions.

Keywords:

Urban drainage, urban flood, flood model, flood exposure, extreme events, Rio de Janeiro

Highlights:

1. A new urban drainage scheme adapted to large-scale models is proposed and tested during major flooding events over Rio de Janeiro, Brazil
2. The drainage system reduces urban flooding by 31-53%, storing up to 2.5 billion m^3 of water during flood peaks across the city
3. Racial minorities are 48% of city residents, but correspond to 53-56% of people exposed to ≥1 meter flood depth during a major event

1. Introduction

Population growth in urban areas, land cover change and climate-induced intensification of extreme hydrometeorological events are main drivers for increasing urban floods globally (Andreadis et al., 2022; Bates, 2022; Merz et al., 2021; Wing et al., 2021). Annually, such a natural hazard results in nearly 4500 deaths and $45.9 billion in economic losses worldwide, totaling over $1 trillion since 1980 (World Water Institute, 2020). Although the ultimate way to mitigate flood risks is through infrastructural investments (e.g., efficient drainage systems, flood control structures, displacement of vulnerable population to low flood risk zones), understanding the hydrological processes driving urban floods is essential for improving decision-making and minimizing exposure (Cappato et al., 2022; Costabile et al., 2020). Urban floodings generally have higher impact on cities in developing countries, particularly those with poor or missing infrastructure.

Over the centuries, Rio de Janeiro city has been hit by extreme flood events, often resulting in fatalities. Spanning 1204 km^2 in area, Rio de Janeiro is located in Southeastern Brazil (Fig. 1) and stands as the second largest city in the country and ranked fifth in Latin America. The city has witnessed a significant urbanization rate in the past few decades, where 6.72 million people live. Part of this urban expansion is composed of informal settlements, mostly in steep hills within the city. More recently, informal settlements have also been spreading in flat flood-prone areas. One of the strongest rainstorms in record, with up to 360mm of rain within 24 hours, caused floodings and landslides in April 2010, killing at least 224 people and making at least 50,000 people homeless across the city and surrounding areas (Reuters, 2010). In the past 2 decades, the municipality has invested in ground-based infrastructure to implement warning and monitoring systems and inform residents on heavy rainfall and landslide risks. A flood monitoring system is still lacking and, although the near annual recurrence, the municipality has little knowledge on how extreme floodings occur across the city and how residents and infrastructure are exposed to flooding.

In 2015, NASA and the city of Rio de Janeiro signed a pioneering partnership to advance natural disaster monitoring capabilities at the city scale. As part of this partnership, the municipality has been providing critical *in situ* data that are combined with NASA tools and datasets to further parameterize and test modeling frameworks (Hurwitz et al., 2020). These models are designed to

monitor and forecast storm-triggered hazards, such as floods and landslides (Getirana et al., 2020b). Motivated by the current absence of a flood monitoring system and activities developed in the framework of NASA-Rio partnership's efforts, a citywide flood monitoring system has been developed using NASA tools. Such a system uses the Hydrological Modeling and Analysis Platform (HyMAP) flood model (Getirana et al., 2012, 2017b) coupled with the Noah with Multi-parameterization (Noah-MP; Niu et al., 2011; Yang et al., 2011) land surface model (LSM) within NASA's Land Information System (LIS) Framework (Kumar et al., 2006). These models have generally been used in continental and global hydrological applications at coarser spatial resolutions (i.e., ≥1km). Hence, an improved representation of physical processes was needed so they could be used at finer city-scale resolutions. Such improvements include the representation of urban drainage in HyMAP.

Over the past several years, the hydrological community has witnessed a continuous refinement of spatial resolutions and physical processes represented in global-scale hydrological models. Such models have acquired the flexibility to navigate across scales and can be used in global and regional domains. However, physical processes normally neglected at large scales may have a non-negligible impact on the water cycle at the kilometer and sub-kilometer resolutions. Urban drainage is an example of such processes. Multiple efforts on integrating surface water and underground drainage models can be found in the literature (e.g., Bertilsson et al., 2019; Bisht et al., 2016; Jang et al., 2007; Mascarenhas and Miguez, 2002; Warwick and Tadepalli, 1991). Smith (2006) provides an overview of early developments. Due to their numeric complexities and data requirements, they are usually applied to small areas, such as a city or parts of it (e.g., Mark et al., 2004). Recent literature shows that there are multiple attempts to integrate hydrology and urban drainage at the city or sub-city scales (Chen et al., 2022; Luo et al., 2022). At larger scales, Bates et al. (2021) analyzes fluvial, pluvial, and coastal flood risks across the conterminous U.S. using a 30-meter resolution flood model. They propose significant improvements to their model, including a refined parameterization of the river network and geometry and local interventions in the flooding system. However, urban drainage is accounted for by simply subtracting a fraction of the rainfall over cities. More recently, Sanders et al. (2022) quantified flood risk and exposure in Los Angeles, California using outputs from a 30-meter spatial resolution hydrodynamic model that were further downscaled to 3 meters. The authors represent the urban drainage by simulating pipes and culverts as surface canals, not as underground drainage.

The goal of this paper is twofold: (1) to describe a new urban drainage parameterization that can be in large-scale flood models, particularly HyMAP; and (2) implement the model in Rio de Janeiro city and evaluate the impacts of the proposed scheme on the simulation of past major floods that took place in the city. Like other flood models, HyMAP was originally designed to represent river and floodplain dynamics. For its implementation over Rio de Janeiro, a new urban drainage scheme had to be developed and coupled to the model. Based on local data, we parameterized urban drainage processes in HyMAP at the city scale. Our holistic approach represents floods from both rainfall and channel overflow, by integrating vertical water and energy balance processes, surface water dynamics over rivers, channels, urban areas, and interactions with an underground drainage system. In this sense, the objective of this paper is to describe and evaluate the proposed urban drainage scheme. The evaluation is performed through model experiments with varying parameterizations during selected major flood events. Based on model outputs, municipal data and demographic surveys, we analyze population and social infrastructure exposure to flooding. Population data is further decomposed based on income, race and ethnicity. Also, another goal of this paper is to document the data requirements and processing steps that can be used as a guideline for further replication in other regions.

2. Modeling framework

This section describes the models and tools used in the development of Rio de Janeiro's flood model. HyMAP and Noah-MP are one-way coupled, which means that, at each time step, gridded surface runoff and baseflow derived from Noah-MP's vertical water and energy balances are transferred to HyMAP and used as inputs to simulate spatially distributed surface water dynamics, but no information is returned from HyMAP to Noah-MP. We assumed that flash floods have little to no impact on the LSM's vertical water balance over urban and impervious areas. Model parameters were processed using the Land surface Data Toolkit (LDT; Arsenault et al., 2018). The next sections provide a full description of the proposed scheme and briefly lists Noah-MP options and parameterizations used in this study. Collection and pre-processing of ground and satellite data used as inputs in HyMAP are fully described in the Appendix sections: section A1 describes the DEM pre-processing, A2 details the methodology to convert point-based to grid-based river geometry data and A3 provides information on the generation of the urban drainage map.

HyMAP

HyMAP is a global scale hydrodynamic model first developed to simulate surface water dynamics in-stream, as well as in floodplains, using the local inertia formulation (Bates et al., 2010; Getirana et al., 2017b), solving the full momentum equation of open channel flow and accounting for a more stable and computationally efficient representation of river flow diffusiveness and inertia of large water mass of deep flow, which is essential for a physically-based representation of wetlands, floodplains, tidal effects and impoundments (Getirana et al., 2021, 2020a). The Courant–Freidrichs–Levy (CFL) condition is used to determine HyMAP's optimal sub timesteps for numerical stability. HyMAP resolves the local inertia formulation unidimensionally (i.e., a unique flow direction is attributed to each grid cell). However, its capability of simulating backwater effects combined with interactions between rivers and floodplains results in a pseudo two-dimensional representation of surface water dynamics. HyMAP has been extensively evaluated in the Amazon basin (Getirana et al., 2013; Getirana and Peters-Lidard, 2013) and adopted as a tool for regional (Getirana et al., 2014; Jung et al., 2017; Kumar et al., 2015, 2016) and global (Getirana et al., 2017a) water cycle studies. The following section describes the proposed urban drainage scheme and changes in the existing parameterization required to adapt HyMAP to represent urban drainage.

Urban drainage scheme

The proposed urban drainage scheme accounts for a modified parameterization of channels, as a way to replace rivers with a urban drainage network within so-called urban grid cells. This means that urban runoff flows thorugh street gutters rather than rivers. Gutter height, H_g [m], is assumed 0.1. Gutter width, W_g [m], is defined as 0.5% of the grid length:

$$W_g = 0.005 \cdot L_b \qquad (1)$$

where L_b [m] stands for the street block size. This corresponds to W_g=0.5m for a hypothetical 100-meter street block.

Water intake is represented by drain inlets with parameterized dimensions, density over urban areas and water intake velocity. Based on these parameters, the model determines the water intake within a grid cell at each time step during a rain event. That water is transferred from the surface to an underground storm drain system (USDS) that is also parameterized. For simplicity, the USDS follows the urban surface flow directions. Water flows in the USDS until it reaches non-urban grid cell or the coast.

Sub-grid processes are simplified following the conceptual representations shown in Fig. 2. In the case of the underground drainage network, we assumed that water storage within a grid cell is defined as the sum of all pipes draining the grid area. We assumed an average squared street block size of L_b=100m and drainage length density, D_d [m/m^2], of 0.02, corresponding to the presence of a single pipe across every street within the urban domain. We also assumed a drain inlet density, D_i [units/m^2], of 8×10^{-4}, corresponding to two drain inlets on each side of a 100-meter street. Drain inlet width and height are defined as W_i=1m and H_i=0.15m, respectively. The total drainage length, L_d [m], maximum water storage capacity in the USDS, $Smax_d$ [m^3], and number of drain inlets, N_i, within a grid cell are defined as:

$$L_d = D_d \cdot A_{grid} \quad (2)$$

$$Smax_d = w_d^2 \cdot L_d \quad (3)$$

$$N_i = D_i \cdot A_{grid} \quad (4)$$

Where A_{grid} [m^2] is the grid cell area and w_d [m] the width of square-shaped underground pipes.

We assumed w_d as one meter. As a result, a hypotetical 200×200m grid cell, with A_{grid}=40,000m^2, would be composed of four blocks, L_d=800m, N_g=32 drain inlets and $Smax_d$=800m^3. Also, as part of sub-grid simplifications, we assumed that the number of USDS outlets N_{out} within a grid cell is defined as:

$$N_{out} = \frac{2 \cdot \sqrt{A_{grid}}}{L_d} \quad (5)$$

At each time step, urban drainage mass balance within a grid cell is defined as

$$S_{d_{t+dt}} = S_{d_t} + \left(I_{d_t} - Qout_{d_t} + \sum_{k=1}^{nUp} Qin_{d_{k,t}}\right) \cdot dt \quad (6)$$

where S_d [m^3] is the drainage water storage at time t [s], and dt stands for the model time step. Qin_d [m^3/s] and $Qout_d$ [m^3/s] are the drainage inflow and outflow, respectively. I_d [m^3/s] is the urban surface vertical flow and the index k stands for the nUp upstream grid cells of the target grid point.

Vertical flow I_d occurs whenever there is water available on the urban surface or water excess in the USDS through a conceptialized dual drainage system (Schmitt et al., 2004), and is defined as

$$if\ S_{d_t} < Smax_d\ ;\ I_{d_t} = N_g \cdot min\left(H_g, h_{s_t}\right) \cdot W_g \cdot v_g \quad (7)$$

$$if\ S_{d_t} \geq Smax_d\ ;\ I_{d_t} = \left(Smax_d - S_{d_t}\right)/dt \quad (8)$$

where h_s [m] is the street water depth and v_g [m/s] the water intake velocity. Although v_g is variable over time as a function of many factors, such as gutter and drain inlet shapes and surface water depth, we assumed a constant value of 2m/s.

Water is routed across the USDS using the kinematic wave equation, considering a rectangular river cross section:

$$Qout_{d_t} = \frac{1}{n_d} \cdot i_d^{1/2} \cdot W_d \cdot h_{d_t}^{5/3} \quad (9)$$

where n_d [-] is surface roughness, i_d [m/m] the drainage longitudinal slope, W_d [m] the total drainage width within a grid cell, defined as $W_d = N_{out} \cdot w_d$, and h_d [m] the drainage water depth. Here, we assumed n_d for concrete pipes as 0.012 (Chow, 1959) and a homogeneous slope i_d =0.003m/m across the USDS. Table 1 summarizes all parameters used in the proposed urban drainage scheme.

At each time step, the remaining urban runoff that was not collected by the USDS is routed thorugh gutters using the local inertia formulation. If the water volume exceeds the gutter capacity, it overflows to streets and sidewalks. Flooded areas are defined by the fraction of streets and sidewalks within a grid that are covered with areas using a DEM-based hypsographic curve.

A Sensitivity analysis of four key parameters was performed for hypothetical storm events over a single 100×100m street block. They are: underground pipe width with a default value of $\boldsymbol{W_d}$=1m, drain inlet width, $\boldsymbol{W_i}$=1m, drain inlet height $\boldsymbol{H_i}$=0.15m and intake velocity v_i=2m/s. Parameter sensitivity was performed by multiplying default values by six factors: 0.25, 0.5, 1, 1.5 and 2. Three rainfall rates were tested by fixing the total amount of rainfall of 420mm, and homogeneously distributing it over different time periods: 2, 4 and 6 hours. Sensitivity was performed in terms of street water depth, in meters. Fig. 3 summarizes the sensitivity analysis. Results show little model sensitivity to rainfall rates and $\boldsymbol{W_d}$ values, except for very small ones (e.g., 0.25m). Indeed, most sensitivity experiments show extreme water depth values for parameters multiplied by 0.25, particularly those with higher rainfall rates. For example, water depth shows no sensitivity to H_i, except for under-dimensioned drain inlet heights under extreme rainfall rates. Results also show that water depth has identical sensitivity to both $\boldsymbol{W_i}$ and v_i, indicating that uncertainties in these two parameters can interchangeably compensated.

Noah-MP

Noah-MP is used to simulate the vertical water and energy balances over the city. The Noah-MP LSM builds upon the well-known Noah LSM (Ek et al., 2003), which has been used in a variety of operational models, applications and research studies. Noah-MP contains four soil layers and different parameterization and physics options, which include different static vegetation and dynamic vegetation schemes, canopy resistance effects, radiation transfer (e.g., two-stream approximation), runoff and groundwater schemes, snow model options, and even crop and urban canopy schemes. We apply the dynamic vegetation scheme, which employs the Ball-Berry canopy and stomatal-resistance option (Ball et al., 1987) and Noah-based soil moisture factor for stomatal resistance. The TOPMODEL simulated groundwater scheme (Niu et al., 2007) is selected, and the Noah-based lower boundary of soil temperature option is applied. Crop and urban physics schemes were not applied at this time since their physics require more review prior to application in LIS. However, to represent more realistic impervious surface responses, land use and soil types related to urban grid-cells were treated as "bedrock", based on suggested parameters in Campbell et al. (2019) and assigning a slightly higher porosity for these points. According to Schueler (2000), the porosity of urban soils varies between 17% to almost 40%. In this sense, an average porosity of 28% to represent urban areas is considered as a valid assumption (Getirana et al., 2020b). The soil configuration simply used the dominant soil texture type map. Other climatology-based vegetation and albedo parameter maps include monthly greenness fraction (Csiszar and Gutman, 1999) and global (snow-free) albedo (Csiszar and Gutman, 1999). Table S1 summarizes the main schemes used in Noah-MP.

a. Meteorological datasets

The modeling system was forced with rainfall fields derived from pluviometric stations and other meteorological fields derived from the operational Global Data Assimilation System (GDAS) meteorological analysis dataset. These datasets are briefly described below.

Pluviometric stations

Rainfall has been measured operationally every 15 minutes since 1997 at 33 pluviometric stations within the city. Their spatial distribution is heterogeneous, mainly concentrated in the more developed eastern portion of the city. The inverse distance squared weighting approach (Shepard, 1968) was used to spatially distribute point-based rainfall observations throughout the city at a

0.002-degree spatial resolution and 30-min time step. Morphology was taken into account following a similar approach suggested in Salvatici et al. (2018), where the domain is divided into sub-regions composed of catchments limited by geomorphological features and the interpolation is performed using only rainfall observations within sub-regions. Here, the city was divided into four catchment-based sub-regions, which are representative of the city's morphology: West, South, Southeast and Northeast. More details on the generation of precipitation fields can be found in (Getirana et al., 2020b).

GDAS

The National Center for Environmental Prediction (NCEP) generates the 6-hourly GDAS analysis product operationally. GDAS uses the Global Forecast System (GFS) atmospheric model and assimilates observations from a variety of surface-based in situ, weather balloon, weather profiler, and buoy networks for each 6-hour analysis update. The native surface fields have evolved from a coarser resolution (~0.7°×0.7°) in 2001, to a finer (~0.117° × 0.117°) one, since the start of 2015, which is still used today. The GDAS surface fields used to force Noah-MP include downward shortwave and longwave radiation, u- and v- wind components, surface temperature, humidity, and pressure. The surface temperature, pressure and humidity fields are further downscaled using a simple lapse-rate approach, as used by different land data assimilation systems (e.g., Cosgrove et al., 2003). Using the environmental lapse rate, estimated at -6.5 K/km, and elevation difference between the GDAS terrain and local topography maps, these meteorological fields are adjusted to the local map elevation height and resolution by applying the equations outlined in Cosgrove et al. (2003).

Evaluation data

The municipality is poor in hydrological data. There is no streamflow data available for model evaluation, flood data started being collected in 2015, but data reports approximated location and time surface runoff accumulates over streets. It is not a comprehensive dataset and evaluating model outputs with it would result in a high number of false positive events. Satellites do not provide cloud-free images during flood events over the city. The Rio de Janeiro State Environmental Institute (INEA) collects river depth data across the state. River depth is measured every 5 to 15 minutes, depending on the location, since 2015 (some locations have data available from 2010). Four gauges are found within our model domain, three of which are located within

289 the city boundaries. They are: Mayrink, Meriti, São Cristovão and Iguaçu (see Fig. 1 for their
290 geographical locations and Table 2 for additional details).

291 ***Model evaluation and experimental design***

292 The urban drainage module with optimal parameters (see Table 1) was evaluated in terms of river
293 depths during three extreme events. These events took place in 5-10 April 2010 (called Event 1
294 hereafter), 5-7 February 2019 (Event 2) and 9-10 April 2019 (Event 3). The model was also
295 evaluated in terms of its sensitivity to key parameters during the same extreme events. Three
296 experiments were performed. Two of them were conducted using *optimal* and *constrained*
297 parameter sets, listed in Table 1. The *constrained* experiment represents a hypothetical under
298 dimensioned or deficient urban drainage system, where drain inlet width, drain inlet density and
299 underground pipe width are defined as half of default values, i.e., W_i=0.5m, D_i=4×10^{-4} units/m^2
300 and W_d=0.5m, respectively. These two experiments are compared in terms of flooded areas and
301 streamflow at key river outlets against another experiment where an urban drainage system is
302 absent (called *nodrain* hereafter).

303 **3. Results**

304 **3.1. Model evaluation**

305 The model evaluation is summarized in Fig. 4. Hourly river depth simulations show overall good
306 agreement with observations across locations and events. Values vary from 0.63 to 0.85, averaging
307 0.77. Such high correlations indicate the model's ability in detecting the timing of extreme events.
308 This is particularly demonstrated in Event 2, where the mean correlation is 0.8. Magnitudes of
309 simulated river depths generally agree with observations, with exceptions. The model highly
310 underestimates river depths at Mayrink, where simulated peaks are as high as 0.12m, while
311 observations reach 0.93m. Such a discrepancy could be explained by possible mismatches between
312 actual and modeled river geometry. This means that the model could be simulating streamflow
313 right, but with a substantially wider channel, river depth amplitudes are lower. Due to the lack of
314 streamflow data, we are unable to check this further. Another possible explanation for this issue is
315 that small headwater catchments (Mayrink gauge is at a high altitude and drains an area of 3.4km^2)
316 may experience high uncertainty in meteorological forcings and land parameters, affecting the
317 simulation of vertical water and energy balance, and directly impacting runoff generation. Indeed,
318 impacts of uncertain meteorological forcings are noticeable in the time series in terms of false or

missing flood peaks. It is also noteworthy that biases exist between simulated and observed river depth, and values vary as a function of location and period. Biases are computed as the difference between simulated and observed river depths at the first time step of events, i.e., negative values indicate lower river depth simulations. In addition to mismatching river geometry, as described above, another explaining factors is the common excess of sedimentation and debris accumulated at the bottom of rivers and canals, which elevates surface river heights.

3.2. Drainage network impacts on urban flood severity

Top panels in Fig. 5 show hourly flood extent time series for three extreme events across urban areas. Permanent open waters (i.e., lakes, canals, and rivers) total 7.8km^2. Simulations show that the representation of a drainage network has major impacts on urban flooding. In the absence of a drainage network (*nodrain* experiment), flood extent peaks (including permanent waters) vary from ~39km^2 to ~47km^2. Flooding substantially drops when an urban drainage is represented in the model: 18-22km^2 (a 48-54% drop) and 25-33km^2 (30-35% drop) for the *optimal* and *constrained* experiments, respectively. Flood peaks are fully absorbed by the *optimal* drainage network, only showing a slight increase. A *constrained* drainage system is insufficient to absorb major peaks, but it floods substantially less than *nodrain*, in addition to showing a quicker flooding decay. Fig. 5 also shows how underground water storage varies over time. On average, the *constrained* drainage network stores 82% of the storm water stored in the *optimal* system. However, that relatively small difference results in additional 7.1-10km^2 flood extent (or 35-46% increase) between *optimal* and *constrained* experiments.

Fig. 6 depicts flood fraction maps at the peak hour of Event 1, i.e., 00:00 – 6 April 2010 GMT. In absence of an urban drainage system represented in the *nodrain* experiment, the city experiences widespread flooding, particularly in flat and low-lying areas over the far-western, central-southern, and eastern portions of the city (Fig. 6a). The *optimal* and *constrained* drainage networks substantially reduce flooded areas in those regions, as shown in Figs. 6b-6c. It is worth noting that, at that time step, positive change in flooding is observed over major rivers and channels draining the city near their outlets (Figs. 6d-6e), when compared to *nodrain*. This is explained by lags in streamflow peaks caused by the drainage system, and not an actual increase in water stored in those rivers and channels during the event. Also, that could be caused by an insufficient storage capacity of the underground drainage system at those locations, resulting in an upflow back to

streets, or underdimensioned urban canals. Similar spatial patterns are observed at peak hours of Event 2 and 3 (Supporting Figs. S1 and S2), with a less pronounced increase in flooding in major rivers and channels.

Urban drainage impacts on streamflow vary as a function of, among other reasons, distribution of urban land cover, topography, storm severity and its spatiotemporal variability. Here, impacts are evaluated at seven locations, shown in Fig. 1. Locations were selected based on its importance draining the city. Their catchment areas vary from 8.29km^2 to 203.8km^2, with urban land use varying from 28% to 65% (see details in Table 2). Fig. 7 shows hourly streamflow time series during the three extreme events at selected locations. Streamflow patterns vary from an event to another. Most of the locations show that peak flows in Event 1 are substantially higher than those observed in Events 2 and 3. These differences are as high as threefold, such as some locations in the eastern (e.g., Maracanã, Carioca and Cunha) and far-western (e.g., Guandu) parts of the city, demonstrating the severity of that event citywide. Those same locations show clear impacts of a drainage system in Event 1, where peaks are smoothened out and delayed by a few hours in the *optimal* and *constrained* experiments. Such a smoothening process reduced peaks by up to 55%. At Maracanã, for example, the flow peak dropped from 245m^3/s to 110m^3/s. At Guandu, in addition to a substantial drop, from 400m^3/s to 190m^3/s, flow peak was delayed by eight hours with an urban drainage system in place. Such differences at Guandu may have been aggravated by a previous wet condition observed at the beginning of the *nodrain* experiment time series. Impacts are less meaningful during Events 2 and 3, and could be explained by a severity threshold below which no substantial change is detected. The exception to the cases described above is Acari, where urban drainage does not show a significant impact on flow peak and timing during any event or streamflow magnitude. No substantial difference in streamflow at selected locations is observed between the *optimal* and *constrained* experiments.

3.3. Exposure of communities and social infrastructure to floods

Flood exposure of communities and social infrastructure has also been analyzed. We combined model outputs with local data to determine how population, schools and hospitals are exposed to flooding at different severity levels, as well as how flood exposure relates to demographics. The spatially distributed population count, and self-declared ethnicity and household income were derived from Brazil's 2010 census (most recent survey to date; https://censo2010.ibge.gov.br/).

Income data was converted to a normalized household income (NHI) index map, varying from zero (lowest income) to 1 (highest income). Details on the computation of NHI is provided in the Supporting Text S1. Racial minorities, defined as non-white Brazilians (i.e., brown, African, Asian, and native Brazilians), were selected to determine flood exposure by ethnicity. Demographic maps were re-gridded to match the model's 0.002-degree spatial resolution. Population, ethnicity, and household income maps do not fully overlap. In this sense, the population map was used as a reference and the other two (NHI and ethnicity) were filled with the averages of immediate neighbors. Education and health care systems are composed of 1540 schools and 688 hospitals, respectively. These systems exclude federal and private schools and hospitals. Spatially distributed NHI, minority populations, education and health care system maps are shown in Fig. 8. There is an imbalance in the distribution of schools and hospitals, which are more densely distributed in the eastern part of the city where the population is also more heavily concentrated. Flood exposure was determined as a function of four flood depth thresholds: ≥0.1m, ≥0.25m, ≥0.5m and ≥1m above the ground elevation. Such thresholds have been defined as flooding levels that may affect walkability and traffic, or damage private property and public infrastructure. Hourly simulations from all experiments were overlapped with demographic, school and hospital maps, and grids were flagged as exposed if, at any time step during a given extreme event, flood depths exceeded each of the selected thresholds. It was assumed that, if a threshold is exceeded, the grid is uniformly flooded at the same depth.

Fig. 9 summarizes the flood exposure analysis. The population exposed to ≥0.1m flood depth varies substantially from an experiment to another. Around 5 million people would be exposed to flooding during Event 1 in a hypothesized absence of a drainage system (i.e., *nodrain* experiment) in the city, representing 75% of residents (Fig. 9a). That count drops to two and one million people – a 60-80% decrease – with *constrained* and *optimal* drainage systems, respectively. They are mostly located in the far-western, central-southern, and eastern parts of the city (see Fig. 10 for spatial distribution of population exposed to flooding thresholds). Those numbers are slightly lower in Events 2 and 3 (Figs. 9b-9c). This demonstrates the importance and positive impacts of a drainage system in reducing flood exposure of urban populations. It also highlights how an optimally dimensioned and well-maintained system can drop flood exposure in the city by half. In more severely flooded areas, i.e., ≥0.25m depth, the exposed population in the *nodrain* experiment is significantly lower, narrowing its differences with the *constrained* experiment in all three events.

The *optimal* experiment also drops to ~600,000 people exposed to ≥0.25m flood depth. In the most severely impacted areas, i.e., ≥0.5m and ≥1m depth, there is little to virtually no difference between experiments. For the latter threshold, the exposed population varies from 200,000 to 300,000 people and they are mainly found near major rivers and channels draining the city (Figs. 10j-10l). This indicates that specific areas of the city will heavily accumulate storm water no matter how the drainage network is parameterized – or not – in the model. It is also worth noting that, in cases where the underground drainage network's slope is steeper than the land surface, the urban drainage system speeds up the urban stormwater runoff directed to the surface water bodies, amplifying and anticipating river peaks. Exceptions are where the land surface slope is steeper than the drainage network. In those cases, impacts on river peaks will vary as a function of the fraction of urban land use within a catchment. It is expected that a small fraction of urban land use in a large catchment will have minor impacts on river dynamics.

Racial minorities and low-income populations are disproportionally exposed to extreme flooding thresholds. Although minorities represent about 48% of residents in the city, they correspond to 53-56% of the population exposed to ≥1m flood depth in Event 1 (Fig. 9d). This is a 10-17% increase compared to the 48% representation among residents exposed to ≥0.1m flood depth. Such an increase in minorities exposed to the most extreme floodings is observed in all three events (Figs. 9d-9f). NHI exposed to flooding vary as an inverse function of exposed minorities (Figs. 9g-9i). Alike minorities, low-income residents are more exposed to extreme flooding thresholds in all events. In Event 1, for example, NHI values drops by up to 25%, from 0.49 at ≥0.1m flood depth threshold to 0.37-0.41 at ≥1m flood depth. These results show a strong correlation between minority and low-income populations and increasing in flood exposure. It is important to note a peculiarity of the city: most of the minorities and low-income populations live in slums, commonly found in elevated steep slopes (Getirana et al., 2020b; Hurwitz et al., 2020). These residents are typically safe from flooding, but exposed to landslides, another frequent and deadly rain-triggered hazard, not analyzed in this study.

Social infrastructure is also exposed to flooding across the city at proportions similar to those experienced by residents. Around 81% of schools and 85% of hospitals would be exposed to flooding during Event 1 in the *nodrain* experiment, corresponding to 1250 and 570 units, respectively (Figs. 9j-9m). Schools and hospitals exposed to flooding substantially drops by 60-85% with *optimal* and *constrained* drainage systems during any event. However, no matter what

441 extreme event it is evaluated, a substantial amount of 32-74 hospitals is exposed to floodings at
442 ≥0.5m depth in any scenario with a drainage network (*optimal* and *constrained*). This demonstrates
443 how vulnerable the city is under extreme flood events, when hospitals should be the safe place to
444 which victims are directed to.

445 **4. Summary and final remarks**

446 Cities are vulnerable to floods. Flood vulnerability tends to increase with urbanization, particularly
447 over flood-prone areas, and intensification of climate-induced hydrological change. Inadequate
448 flood control infrastructure makes major cities more vulnerable, especially those found in
449 developing countries and exposed to heavy rainfall seasons. Rio de Janeiro city is no exception to
450 such issues. Recurring extreme flood events over the past several decades and the absence of a
451 flood monitoring system have motivated the development of the proposed urban drainage scheme.
452 The developments presented in this paper are the result of a multi-year-long partnership between
453 NASA and local agencies supporting urban development and climate resiliency. The proposed
454 modeling system is built upon NASA's LIS framework and HyMAP global-scale flood model.
455 Based on local expertise and high-resolution data, we were able to downscale the HyMAP to ~200
456 meters over the city with refined urban hydrology processes and parameters. Based on experiments
457 with three different parameterizations, we found that the proposed scheme was able to reduce the
458 extent of simulated urban floodings during selected major events by transferring storm water from
459 the surface to the underground drainage system. As a result, there is a 60-80% drop in residents
460 and social infrastructure – schools and hospitals – exposed to flooding. An analysis of exposure to
461 flood severity showed that minorities and low-income populations are disproportionally more
462 exposed to severe floodings.

463 Results demonstrate that the system can be used in a routine manner and support decision-making
464 processes at the city scale, as well as drainage system design and efficiency evaluation. This is an
465 ongoing work and next steps are the transfer, automation, and operationalization of the urban flood
466 model. Indeed, data access and availability are essential for an accurate representation of urban
467 drainage impacts on floodings. Rio de Janeiro has invaluable information on topography, land use,
468 hydrography, real-time rainfall, and demographics. However, the lack of consistent river and
469 channel discharge time series, and comprehensive maps of flood extent and duration prevented us
470 from performing a full model evaluation against known extreme events. Hence, there is a need for

more validation data to support a robust characterization of flooding that can be used in further model development. Information on the urban drainage network, its spatially distributed features, as well as operation of local flood control structures, were not available at the time the model was developed. As a result, there is room for model improvement and refinement as data become available. Due to the high parameterization of urban drainage processes, the proposed scheme allows the use of spatially homogeneous parameters or customized and spatially distributed information, upon urban drainage data availability.

HyMAP is based on the local inertia formulation and optimal sub timesteps defined using the CFL condition may increase exponentially with spatial resolution (i.e., the finer the spatial resolution is, the finer the time step will be). As a result, we opted for a ~200-meter spatial resolution as a compromise between spatial precision and computational costs. Although it is acknowledged the existence of scaling issues in urban drainage modeling (Ichiba et al., 2018), HyMAP contains sub-grid information allowing us to further downscale model outputs. As part of the automation and operationalization of the system, a downscaling algorithm will process HyMAP outputs and sub-grid elevation data, including bare ground and built elevation, resulting in flood extents at 10-meter spatial resolution.

Here, exposed population is computed by overlapping simulated flood depth maps with grid-based population counts, assuming that residents within grids are equally impacted. Our evaluation also neglects impacts on mobility, assets and other infrastructures that could influence the livelihood beyond the grid point. These limitations can be addressed in future work through a sub-grid analysis using downscaled flood maps. The model can also be improved by accounting for flood control structures and the canalization of numerous rivers across the city. Sea levels were considered constant in this study. Varying sea levels would account for the compounding effects of high tides and storms surges on flood events. Neglecting these processes and infrastructures may have resulted in an underestimation of simulated flood extent and exposure.

Lessons learned during the development, transfer, automation, and operationalization steps will support their replicability and scalability to other cities in need for similar monitoring systems. Satellite data can be a viable alternative for the absence of ground measurements. NASA's Global Precipitation Measurement (GPM) mission provides us with global rainfall estimates at 30-min time step and 0.1° spatial resolution (Skofronick-Jackson et al., 2018), and can be used as an

alternative source of near real-time precipitation data over poorly equipped cities (Getirana et al., 2020b). However, care must be taken to closely evaluate the GPM performance over cities to ensure reasonable representation of urban precipitation patterns. High-resolution DEMs are available at resolutions as fine as 12 meters globally, such as TanDEM-X (Alonso-Gonzalez et al., 2021), and can also be used in the absence of Lidar or ground based topography data. However, vertical errors and lack of bare ground information and building elevations may add uncertainty to urban flood modeling. In the absence of local urban land use data, global-scale satellite, such as the TanDEM-X FNF dataset at 50m (Martone et al., 2018) and NASA's Black Marble night-time lights product at 500m (Román et al., 2018), can be used as proxies for urban extents.

Acknowledgements

This research was funded by the NASA Applied Sciences – Disasters Program. Computing resources supporting this work were provided by the NASA High-End Computing (HEC) Program through the NASA Center for Climate Simulation (NCCS) at NASA Goddard Space Flight Center.

Appendix

Here, we describe datasets and data pre-processing steps needed as inputs into the flood model. We focus on the (1) digital elevation model pre-processing, (2) river and channel geometry and roughness parameterization, and (3) urban drainage map generation.

A1. Digital elevation model pre-processing

Lidar data is available for the municipality and was acquired through an aerial survey in the second half of 2019, with a raw density of eight points per square meter. Point-based cloud data was filtered for ground-only returns and interpolated as a 15-cm spatial resolution digital terrain model map. The domain outside the city boundaries was filled with MERIT DEM. Both datasets were resampled to 10 meters. The Lidar data was converted from Brazil's Imbituba vertical datum to EGM96, matching MERIT's. Remaining vertical biases between resampled datasets were addressed by computing differences at Lidar grid elevations below 50 meters using a 400-meter buffer along the city boundaries. Differences above 50-meter elevation were neglected as floods are more likely to occur at low elevations and (ii) the averaged bias can be negatively impacted by large differences at high elevations. The 1.23-meter bias was added to the Lidar DEM. A stream burning approach (e.g., Getirana et al., 2009a, 2009b) was used to correct flow directions over flat

areas. We visually compared DEM-based flow directions with a vector-based hydrography dataset to identify and select inconsistent locations where corrections were needed. Selected DEM grids were "burned" by subtracting a constant elevation of 50 meters. A hydrologically consistent DEM was created, and flow directions and the drainage network were acquired using DEM processing algorithms available on ArcGIS Pro. Fig. A1a shows the final DEM at 10-meter resolution, and Figs. A1b-A1e show details of the DEM with and without edifications and resulting flow directions and drainage network maps.

A2. Methodology to convert point-based to grid-based river geometry data

Grid-based river geometry was generated following Getirana's et al. (2023) approach, which is briefly described in this section. Ground-based cross-sectional channel bathymetry measurements are available at 29 locations across the city. These measurements were converted to channel widths and depths, assuming rectangular cross sections. Additional 260 channel width measurements were manually acquired on Google Earth. Fig. A2a shows their locations. We used the 10-meter hydrological network, described in Appendix A1, as the baseline to spatialize point-based channel geometry parameters. First, we attributed W_r and A_r values to grid points representing corresponding rivers and channels. Then, channel geometry at outlets and headwaters were empirically defined. A minimum river width was used at headwater grid points, defined as W_{min}=0.1m. For catchments with at least two data grid points, we used the most downstream point to determine outlet width, W_{outlet} [m], and height, H_{outlet} [m], by assuming these parameters are constant between these two grid points. For catchments with one or no data grid point, W_{outlet} and H_{outlet} were determined through power law relationships with drainage area, A_d [km^2]. These relationships are defined as follows:

$$H_{outlet} = 0.5193 \cdot A_d^{5.726} \quad \text{(A1)}$$

$$W_{outlet} = 0.468 \cdot A_d^{0.656} \quad \text{(A2)}$$

Ten-meter resolution river geometry maps were upscaled to 0.002° using the Flexible Location of Waterways (FLOW) method (Yamazaki et al., 2009). Figs. A2b and A2c show citywide upscaled W_r and H_r, respectively. Surface water flow roughness was assumed as 0.015 on urban areas (e.g.,

asphalt and concrete) and 0.03 over river, channels, and other land covers (Chow, 1959). Fig. A2d shows the surface roughness map at 0.002°.

A3. Urban drainage map

The urban drainage map used in the HyMAP merges three data sources: the vector-based 2018 municipal land use map (Fig. A3a), global TanDEM-X Forest/Non-Forest Map (FNF) data at 50-meter spatial resolution (Martone et al., 2018) (Fig. A3b) and the 0.002° river network at 1.5km^2 threshold (Fig. A3c). Both land use and TanDEM-X FNF maps were resampled to 0.002° and merged. The merging process included urban area grids from both datasets. Finally, grids flagged as rivers were masked out from the urban area, resulting in the urban drainage map used in HyMAP (Fig. A3d).

Open Research

LIS parameters used in this study are available on https://figshare.com/articles/dataset/lis_input_200m_noahmp401_hymap_urban_hybrid_nc/21842943. The GDAS meteorological analysis dataset is distributed by NCEP through https://www.ncei.noaa.gov/products/weather-climate-models/global-data-assimilation, local pluviometric data through http://alertario.rio.rj.gov.br/download/dados-pluviometricos/, municipal schools and health care data https://www.data.rio/datasets/PCRJ::escolas-municipais/explore?location=-22.911184%2C-43.415750%2C11.80 and https://www.data.rio/datasets/unidades-de-sa%C3%BAde-municipais-1/explore?location=-22.913960%2C-43.412808%2C11.82, respectively, polygon-based normalized household income index https://www.data.rio/datasets/PCRJ::%C3%ADndice-de-desenvolvimento-social-da-cidade-do-rio-de-janeiro-2010/about. The 2018 municipal land use map is available on https://www.data.rio/datasets/cobertura-vegetal-e-uso-da-terra-2018/explore?location=-22.746306%2C-43.444850%2C6.27 and the Global TanDEM-X FNF data on https://geoservice.dlr.de/web/dataguide/fnf50/. River depth observations are made available by INEA through https://drive.google.com/drive/folders/1jOfCAhb8llozzsAOE-KW9NJYC_ivcgNx?usp=share_link.

Code Availability

LIS and LDT are freely available through https://github.com/NASA-LIS/LISF.

References

Alonso-Gonzalez, A., Martinez, N.G., Hajnsek, I., Revenga, P.C., Bonilla, M.J.G., Grigorov, C., Roth, A., Marschalk, U., Vazquez, N.C., Cuerda, J.M., Rodriguez, M.G., 2021. Joint PAZ & TanDEM-X Mission Interferometric Experiments: Interoperability and Products. IEEE J. Sel. Top. Appl. Earth Obs. Remote Sens. 14, 6069–6082. https://doi.org/10.1109/JSTARS.2021.3084401

Andreadis, K.M., Wing, O.E.J., Colven, E., Gleason, C.J., Bates, P.D., Brown, C.M., 2022. Urbanizing the floodplain: global changes of imperviousness in flood-prone areas. Environ. Res. Lett. 17, 104024. https://doi.org/10.1088/1748-9326/ac9197

Arsenault, K.R., Kumar, S. V., Geiger, J. V., Wang, S., Kemp, E., Mocko, D.M., Beaudoing, H.K., Getirana, A., Navari, M., Li, B., Jacob, J., Wegiel, J., Peters-Lidard, C.D., 2018. The Land surface Data Toolkit (LDT v7.2) - A data fusion environment for land data assimilation systems. Geosci. Model Dev. 11, 3605–3621. https://doi.org/10.5194/gmd-11-3605-2018

Ball, J.T., Woodrow, I.E., Berry, J.A., 1987. A Model Predicting Stomatal Conductance and its Contribution to the Control of Photosynthesis under Different Environmental Conditions, in: Progress in Photosynthesis Research. Springer Netherlands, Dordrecht, pp. 221–224. https://doi.org/10.1007/978-94-017-0519-6_48

Bates, P., 2022. Uneven burden of urban flooding. Nat. Sustain. https://doi.org/10.1038/s41893-022-01000-9

Bates, P.D., Horritt, M.S., Fewtrell, T.J., 2010. A simple inertial formulation of the shallow water equations for efficient two-dimensional flood inundation modelling. J. Hydrol. 387, 33–45. https://doi.org/10.1016/j.jhydrol.2010.03.027

Bates, P.D., Quinn, N., Sampson, C., Smith, A., Wing, O., Sosa, J., Savage, J., Olcese, G., Neal, J., Schumann, G., Giustarini, L., Coxon, G., Porter, J.R., Amodeo, M.F., Chu, Z., Lewis-Gruss, S., Freeman, N.B., Houser, T., Delgado, M., Hamidi, A., Bolliger, I., McCusker, K., Emanuel, K., Ferreira, C.M., Khalid, A., Haigh, I.D., Couasnon, A., Kopp, R., Hsiang, S., Krajewski, W.F., 2021. Combined Modeling of US Fluvial, Pluvial, and Coastal Flood Hazard Under Current and Future Climates. Water Resour. Res. 57. https://doi.org/10.1029/2020WR028673

Bertilsson, L., Wiklund, K., de Moura Tebaldi, I., Rezende, O.M., Veról, A.P., Miguez, M.G., 2019. Urban flood resilience – A multi-criteria index to integrate flood resilience into urban planning. J. Hydrol. 573, 970–982. https://doi.org/10.1016/j.jhydrol.2018.06.052

Bisht, D.S., Chatterjee, C., Kalakoti, S., Upadhyay, P., Sahoo, M., Panda, A., 2016. Modeling urban floods and drainage using SWMM and MIKE URBAN: a case study. Nat. Hazards 84, 749–776. https://doi.org/10.1007/s11069-016-2455-1

Campbell, P.C., Bash, J.O., Spero, T.L., 2019. Updates to the Noah Land Surface Model in WRF-CMAQ to Improve Simulated Meteorology, Air Quality, and Deposition. J. Adv. Model. Earth Syst. 11, 231–256. https://doi.org/10.1029/2018MS001422

626 Cappato, A., Baker, E.A., Reali, A., Todeschini, S., Manenti, S., 2022. The role of modeling
627 scheme and model input factors uncertainty in the analysis and mitigation of backwater
628 induced urban flood-risk. J. Hydrol. 614, 128545.
629 https://doi.org/10.1016/j.jhydrol.2022.128545

630 Chen, W., Wu, H., Kimball, J.S., Alfieri, L., Nanding, N., Li, X., Jiang, L., Wu, W., Tao, Y.,
631 Zhao, S., Zhong, W., 2022. A Coupled River Basin-Urban Hydrological Model (DRIVE-
632 Urban) for Real-Time Urban Flood Modeling. Water Resour. Res. 58.
633 https://doi.org/10.1029/2021WR031709

634 Chow, V. Te, 1959. Open Channel Hydraulics. McGraw-Hill, New York, New York, USA.

635 Cosgrove, B.A., Lohmann, D., Mitchell, K.E., Houser, P.R., Wood, E.F., Schaake, J.C., Robock,
636 A., Marshall, C., Sheffield, J., Duan, Q., Luo, L., Higgins, R.W., Pinker, R.T., Tarpley, J.D.,
637 Meng, J., 2003. Real-time and retrospective forcing in the North American Land Data
638 Assimilation System (NLDAS) project. J. Geophys. Res. Atmos. 108, 2002JD003118.
639 https://doi.org/10.1029/2002JD003118

640 Costabile, P., Costanzo, C., De Lorenzo, G., Macchione, F., 2020. Is local flood hazard
641 assessment in urban areas significantly influenced by the physical complexity of the
642 hydrodynamic inundation model? J. Hydrol. 580, 124231.
643 https://doi.org/10.1016/j.jhydrol.2019.124231

644 Csiszar, I., Gutman, G., 1999. Mapping global land surface albedo from NOAA AVHRR. J.
645 Geophys. Res. Atmos. 104, 6215–6228. https://doi.org/10.1029/1998JD200090

646 Ek, M.B., Mitchell, K.E., Lin, Y., Rogers, E., Grunmann, P., Koren, V., Gayno, G., Tarpley,
647 J.D., 2003. Implementation of Noah land surface model advances in the National Centers
648 for Environmental Prediction operational mesoscale Eta model. J. Geophys. Res. Atmos.
649 108. https://doi.org/10.1029/2002JD003296

650 Getirana, A., Bonnet, M.-P., Martinez, J.-M., 2009a. Evaluating parameter effects in a DEM
651 “burning” process based on land cover data. Hydrol. Process. 23.
652 https://doi.org/10.1002/hyp.7303

653 Getirana, A., Bonnet, M.-P., Rotunno Filho, O.C., Mansur, W.J., 2009b. Improving hydrological
654 information acquisition from DEM processig in floodplains. Hydrol. Process. 23.
655 https://doi.org/10.1002/hyp.7167

656 Getirana, A., Boone, A., Yamazaki, D., Decharme, B., Papa, F., Mognard, N., 2012. The
657 hydrological modeling and analysis platform (HyMAP): Evaluation in the Amazon basin. J.
658 Hydrometeorol. 13. https://doi.org/10.1175/JHM-D-12-021.1

659 Getirana, A., Boone, A., Yamazaki, D., Mognard, N., 2013. Automatic parameterization of a
660 flow routing scheme driven by radar altimetry data : Evaluation in the Amazon basin. Water
661 Resour. Res. 49. https://doi.org/10.1002/wrcr.20077

662 Getirana, A., Dutra, E., Guimberteau, M., Kam, J., Li, H.Y., Decharme, B., Zhang, Z., Ducharne,
663 A., Boone, A., Balsamo, G., Rodell, M., Toure, A.M., Xue, Y., Peters-Lidard, C.D., Kumar,

S. V., Arsenault, K., Drapeau, G., Leung, L.R., Ronchail, J., Sheffield, J., 2014. Water balance in the amazon basin from a land surface model ensemble. J. Hydrometeorol. 15, 2586–2614. https://doi.org/10.1175/JHM-D-14-0068.1

Getirana, A., Jung, H.C., Van Den Hoek, J., Ndehedehe, C.E., 2020a. Hydropower dam operation strongly controls Lake Victoria's freshwater storage variability. Sci. Total Environ. 726, 138343. https://doi.org/10.1016/j.scitotenv.2020.138343

Getirana, A., Kirschbaum, D., Mandarino, F., Ottoni, M., Khan, S., Arsenault, K., 2020b. Potential of GPM IMERG precipitation estimates to monitor natural disaster triggers in urban areas: The case of Rio de Janeiro, Brazil. Remote Sens. 12, 1–20. https://doi.org/10.3390/rs12244095

Getirana, A., Kumar, S., Girotto, M., Rodell, M., 2017a. Rivers and Floodplains as Key Components of Global Terrestrial Water Storage Variability. Geophys. Res. Lett. 44, 10,359-10,368. https://doi.org/10.1002/2017GL074684

Getirana, A., Kumar, S., Konapala, G., Ndehedehe, C.E., 2021. Impacts of fully coupling land surface and flood models on the simulation of large wetlands' water dynamics: the case of the Inner Niger Delta. J. Adv. Model. Earth Syst. https://doi.org/10.1029/2021MS002463

Getirana, A., Kumar, S., Konapala, G., Nie, W., Locke, K., Loomis, B., Birkett, C., Ricko, M., Simard, M., 2023. Climate and human impacts on hydrological processes and flood risk in southern Louisiana. Water Resour. Res.

Getirana, A., Peters-Lidard, C., 2013. Estimating water discharge from large radar altimetry datasets. Hydrol. Earth Syst. Sci. 17. https://doi.org/10.5194/hess-17-923-2013

Getirana, A., Peters-Lidard, C., Rodell, M., Bates, P.D., 2017b. Trade-off between cost and accuracy in large-scale surface water dynamic modeling. Water Resour. Res. https://doi.org/10.1002/2017WR020519

Hurwitz, M., Braneon, C., Kirschbaum, D., Mandarino, F., Mansour, R., 2020. Earth Observations Informing Cities' Operations and Planning. Eos (Washington. DC). 101. https://doi.org/10.1029/2020EO146808

Ichiba, A., Gires, A., Tchiguirinskaia, I., Schertzer, D., Bompard, P., Ten Veldhuis, M.-C., 2018. Scale effect challenges in urban hydrology highlighted with a distributed hydrological model. Hydrol. Earth Syst. Sci. 22, 331–350. https://doi.org/10.5194/hess-22-331-2018

Jang, S., Cho, M., Yoon, J., Yoon, Y., Kim, S., Kim, G., Kim, L., Aksoy, H., 2007. Using SWMM as a tool for hydrologic impact assessment. Desalination 212, 344–356. https://doi.org/10.1016/j.desal.2007.05.005

Jung, H.C., Getirana, A., Policelli, F., McNally, A., Arsenault, K.R., Kumar, S., Tadesse, T., Peters-Lidard, C.D., 2017. Upper Blue Nile basin water budget from a multi-model perspective. J. Hydrol. 555, 535–546. https://doi.org/10.1016/j.jhydrol.2017.10.040

Kumar, S., Peters-Lidard, C.D., Arsenault, K.R., Getirana, A., Mocko, D., Liu, Y., 2015. Quantifying the Added Value of Snow Cover Area Observations in Passive Microwave

Snow Depth Data Assimilation. J. Hydrometeorol. 16, 1736–1741. https://doi.org/10.1175/jhm-d-15-0021.1

Kumar, S. V., Peters-Lidard, C.D., Tian, Y., Houser, P.R., Geiger, J., Olden, S., Lighty, L., Eastman, J.L., Doty, B., Dirmeyer, P., Adams, J., Mitchell, K., Wood, E.F., Sheffield, J., 2006. Land information system: An interoperable framework for high resolution land surface modeling. Environ. Model. Softw. 21, 1402–1415. https://doi.org/10.1016/j.envsoft.2005.07.004

Kumar, S. V., Zaitchik, B.F., Peters-Lidard, C.D., Rodell, M., Reichle, R., Li, B., Jasinski, M., Mocko, D., Getirana, A., De Lannoy, G., Cosh, M.H., Hain, C.R., Anderson, M., Arsenault, K.R., Xia, Y., Ek, M., 2016. Assimilation of Gridded GRACE terrestrial water storage estimates in the North American land data assimilation system. J. Hydrometeorol. 17, 1951–1972. https://doi.org/10.1175/JHM-D-15-0157.1

Luo, P., Luo, M., Li, F., Qi, X., Huo, A., Wang, Z., He, B., Takara, K., Nover, D., Wang, Y., 2022. Urban flood numerical simulation: Research, methods and future perspectives. Environ. Model. Softw. 156, 105478. https://doi.org/10.1016/j.envsoft.2022.105478

Mark, O., Weesakul, S., Apirumanekul, C., Aroonnet, S.B., Djordjević, S., 2004. Potential and limitations of 1D modelling of urban flooding. J. Hydrol. 299, 284–299. https://doi.org/10.1016/j.jhydrol.2004.08.014

Martone, M., Rizzoli, P., Wecklich, C., González, C., Bueso-Bello, J.-L., Valdo, P., Schulze, D., Zink, M., Krieger, G., Moreira, A., 2018. The global forest/non-forest map from TanDEM-X interferometric SAR data. Remote Sens. Environ. 205, 352–373. https://doi.org/10.1016/j.rse.2017.12.002

Mascarenhas, F.C.B., Miguez, M.G., 2002. Urban Flood Control through a Mathematical Cell Model. Water Int. 27, 208–218. https://doi.org/10.1080/02508060208686994

Merz, B., Blöschl, G., Vorogushyn, S., Dottori, F., Aerts, J.C.J.H., Bates, P., Bertola, M., Kemter, M., Kreibich, H., Lall, U., Macdonald, E., 2021. Causes, impacts and patterns of disastrous river floods. Nat. Rev. Earth Environ. 2, 592–609. https://doi.org/10.1038/s43017-021-00195-3

Niu, G.-Y., Yang, Z.-L., Dickinson, R.E., Gulden, L.E., Su, H., 2007. Development of a simple groundwater model for use in climate models and evaluation with Gravity Recovery and Climate Experiment data. J. Geophys. Res. 112, D07103. https://doi.org/10.1029/2006JD007522

Niu, G.Y., Yang, Z.L., Mitchell, K.E., Chen, F., Ek, M.B., Barlage, M., Kumar, A., Manning, K., Niyogi, D., Rosero, E., Tewari, M., Xia, Y., 2011. The community Noah land surface model with multiparameterization options (Noah-MP): 1. Model description and evaluation with local-scale measurements. J. Geophys. Res. Atmos. 116, 1–19. https://doi.org/10.1029/2010JD015139

Reuters, 2010. Brazil flood death toll rises to 224 - officials [WWW Document]. Reuters. URL https://www.reuters.com/article/idUSN12106727 (accessed 1.14.23).

Román, M.O., Wang, Z., Sun, Q., Kalb, V., Miller, S.D., Molthan, A., Schultz, L., Bell, J., Stokes, E.C., Pandey, B., Seto, K.C., Hall, D., Oda, T., Wolfe, R.E., Lin, G., Golpayegani, N., Devadiga, S., Davidson, C., Sarkar, S., Praderas, C., Schmaltz, J., Boller, R., Stevens, J., Ramos González, O.M., Padilla, E., Alonso, J., Detrés, Y., Armstrong, R., Miranda, I., Conte, Y., Marrero, N., MacManus, K., Esch, T., Masuoka, E.J., 2018. NASA's Black Marble nighttime lights product suite. Remote Sens. Environ. 210, 113–143. https://doi.org/10.1016/j.rse.2018.03.017

Salvatici, T., Tofani, V., Rossi, G., D'Ambrosio, M., Tacconi Stefanelli, C., Masi, E.B., Rosi, A., Pazzi, V., Vannocci, P., Petrolo, M., Catani, F., Ratto, S., Stevenin, H., Casagli, N., 2018. Application of a physically based model to forecast shallow landslides at a regional scale. Nat. Hazards Earth Syst. Sci. 18, 1919–1935. https://doi.org/10.5194/nhess-18-1919-2018

Sanders, B.F., Schubert, J.E., Kahl, D.T., Mach, K.J., Brady, D., AghaKouchak, A., Forman, F., Matthew, R.A., Ulibarri, N., Davis, S.J., 2022. Large and inequitable flood risks in Los Angeles, California. Nat. Sustain. https://doi.org/10.1038/s41893-022-00977-7

Schmitt, T.G., Thomas, M., Ettrich, N., 2004. Analysis and modeling of flooding in urban drainage systems. J. Hydrol. 299, 300–311. https://doi.org/10.1016/j.jhydrol.2004.08.012

Schueler, T.R., 2000. The Compaction of Urban Soils, in: Schueler, T.R., Holland, H.K. (Eds.), The Practice of Watershed Protection. Center for Watershed Protection, Ellicott City, MD, pp. 661–665.

Shepard, D., 1968. A two-dimensional interpolation function for irregularly-spaced data, in: Proceedings of the 1968 23rd ACM National Conference On -. ACM Press, New York, New York, USA, pp. 517–524. https://doi.org/10.1145/800186.810616

Skofronick-Jackson, G., Kirschbaum, D., Petersen, W., Huffman, G., Kidd, C., Stocker, E., Kakar, R., 2018. The Global Precipitation Measurement (GPM) mission's scientific achievements and societal contributions: reviewing four years of advanced rain and snow observations. Q. J. R. Meteorol. Soc. 144, 27–48. https://doi.org/10.1002/qj.3313

Smith, M., 2006. Comment on 'Potential and limitations of 1D modeling of urban flooding' by O. Mark et al. [J. Hydrol. 299 (2004) 284-299]. J. Hydrol. 321, 1–4. https://doi.org/10.1016/j.jhydrol.2005.07.036

Warwick, J.J., Tadepalli, P., 1991. Efficacy of SWMM Application. J. Water Resour. Plan. Manag. 117, 352–366. https://doi.org/10.1061/(ASCE)0733-9496(1991)117:3(352)

Wing, O.E.J., Smith, A.M., Marston, M.L., Porter, J.R., Amodeo, M.F., Sampson, C.C., Bates, P.D., 2021. Simulating historical flood events at the continental scale: observational validation of a large-scale hydrodynamic model. Nat. Hazards Earth Syst. Sci. 21, 559–575. https://doi.org/10.5194/nhess-21-559-2021

World Water Institute, 2020. RELEASE: New Data Shows Millions of People, Trillions in Property at Risk from Flooding — But Infrastructure Investments Now Can Significantly Lower Flood Risk [WWW Document]. URL https://www.wri.org/news/release-new-data-shows-millions-people-trillions-property-risk-flooding-infrastructure

780 Yamazaki, D., Oki, T., Kanae, S., 2009. Deriving a global river network map and its sub-grid
781 topographic characteristics from a fine-resolution flow direction map. Hydrol. Earth Syst.
782 Sci. 13, 2241–2251. https://doi.org/10.5194/hess-13-2241-2009

783 Yang, Z.-L., Niu, G.-Y., Mitchell, K.E., Chen, F., Ek, M.B., Barlage, M., Longuevergne, L.,
784 Manning, K., Niyogi, D., Tewari, M., Xia, Y., 2011. The community Noah land surface
785 model with multiparameterization options (Noah-MP): 2. Evaluation over global river
786 basins. J. Geophys. Res. Atmos. 116. https://doi.org/10.1029/2010JD015140

787

788 **Table 1**. Values and description for parameters used in the proposed urban drainage scheme.

Symbol [unit]	**Description**	**Optimal values**	**Constrained values**
L_b [m]	Street block length	100	100
W_g [m]	Gutter width	$0.005 \cdot L_b$	$0.005 \cdot L_b$
H_g [m]	Gutter height	0.1	0.1
W_i [m]	**Drain inlet width**	**1**	**0.5**
H_i [m]	Drain inlet height	0.15	0.15
D_i [units/m^2]	**Drain inlet density**	**8×10^{-4}**	**4×10^{-4}**
v_i [m.s^{-1}]	Drain water intake velocity	2	2
W_d [m]	**Underground pipe width**	**1**	**0.5**
D_d [m.m^{-2}]	Underground pipe length density	0.02	0.02
n_d [-]	Underground pipe roughness coefficient	0.012	0.012
i_d [m.m^{-1}]	Underground pipe slope	0.003	0.003

789

Table 2. Selected urban river catchments. The second column defines locations used to evaluate river depth or discharge.

River/canal	River depth (H) or discharge (Q) evaluation	Longitude	Latitude	Drainage area (km^2)	Urban area (%)
Maracanã	Q	-43.21	-22.9	41.94	39
Acari	Q	-43.34	-22.82	101.73	57
Piraquê	Q	-43.6	-22.97	72.97	30
Arroio Fundo	Q	-43.36	-22.97	56.88	32
Carioca	Q	-43.17	-22.94	8.29	41
Cunha	Q	-43.23	-22.87	56.96	65
Guandu	Q	-43.78	-22.93	203.8	28
Mayrink	H	-43.28	-22.96	3.4	0
Meriti	H	-43.37	-22.8	32.2	45
Iguaçu	H	-43.46	-22.75	40.6	30
São Cristovão	H	-43.22	-22.91	23.8	59

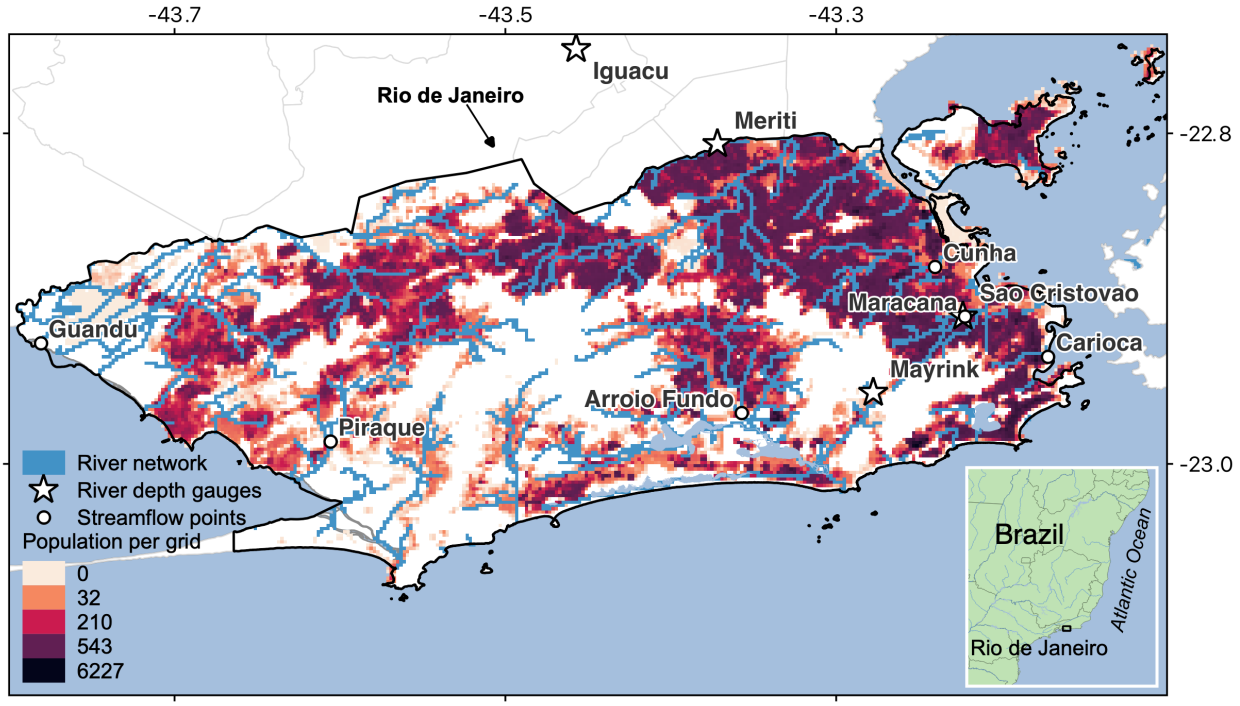

793

794 **Figure 1.** Study domain. Geographic location of Rio de Janeiro city, Brazil, population and river
795 network maps at 0.002° spatial resolution, four river depth gauges and seven locations where
796 simulated streamflow is evaluated. Maracana gauge is also part of the streamflow evaluation,
797 although no streamflow observation is available. Iguacu gauge is outside the city boundaries, but
798 within our model domain.

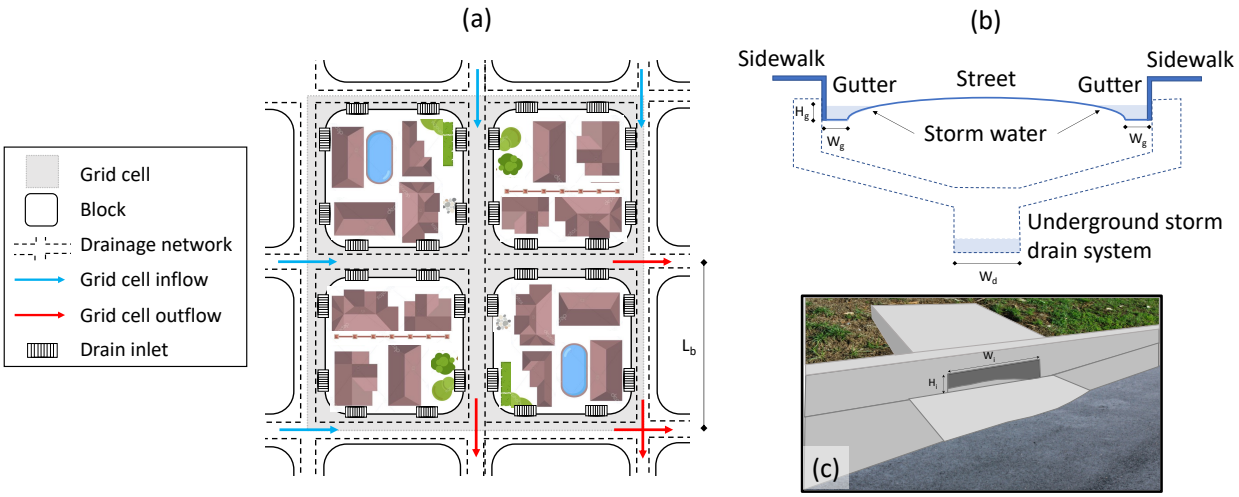

799

800 **Figure 2**. Schematic of the proposed urban drainage scheme within a squared 200×200-meter grid
801 cell: (a) conceptual sub-grid representation of the urban drainage network, including the
802 distribution of drain inlets and sub-grid cell inflow and outflow pathways (street block sizes are
803 assumed as 100×100 meters); (b) conceptual representation of the street drainage and underground
804 storm drain systems, including underground pipe width (W_d) gutter heigth (H_g) and width (W_g);
805 and (c) conceptual drain inlet and its height (H_i) and width (W_i).

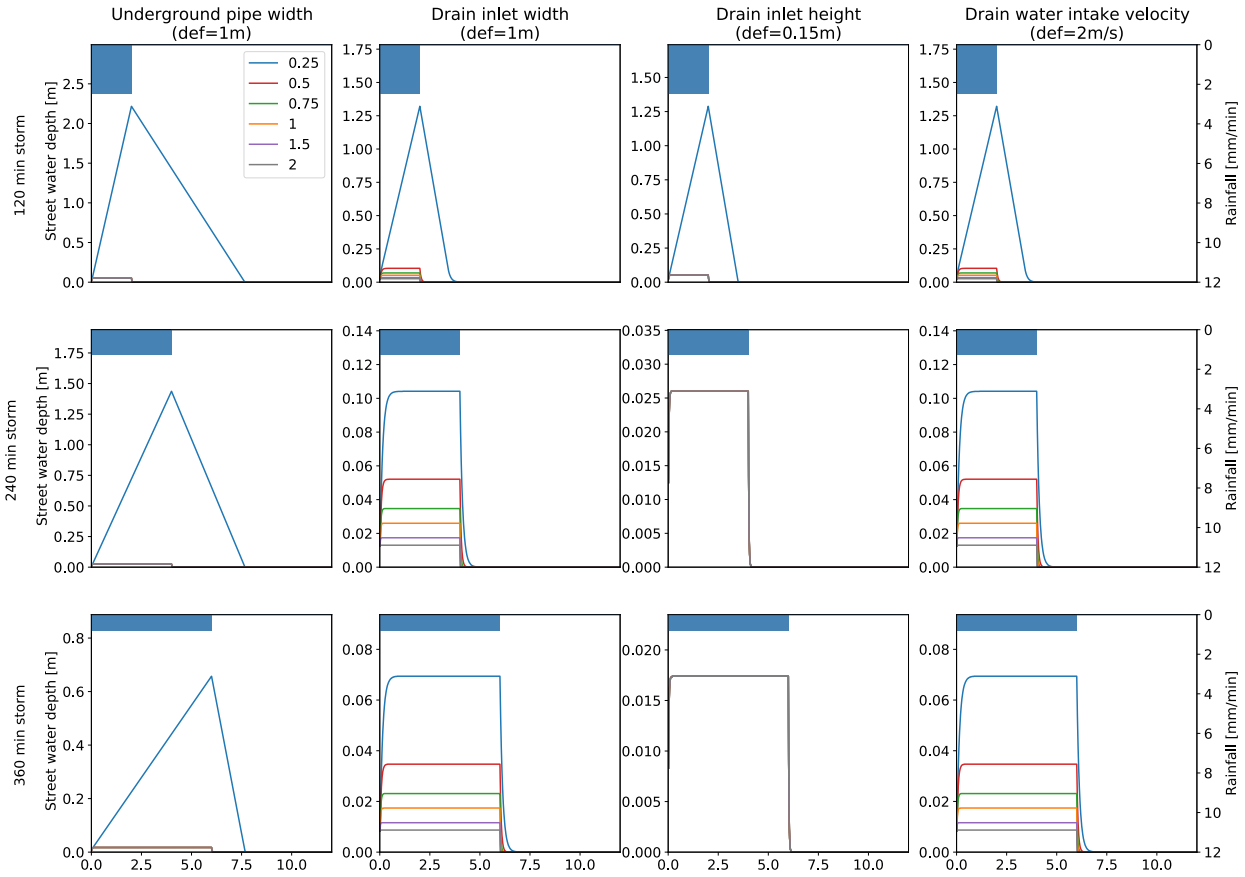

806

807 **Figure 3.** Sensitivity analysis of key parameters for hypothetical storm events over a single
808 100×100m street block. Parameters tested are pipe dimension, gutter width and height and intake
809 velocity. Experiments are performed as a function of factors multiplying default values provided
810 in Table 1. Six factors are used: 0.25, 0.5, 1, 1.5 and 2.

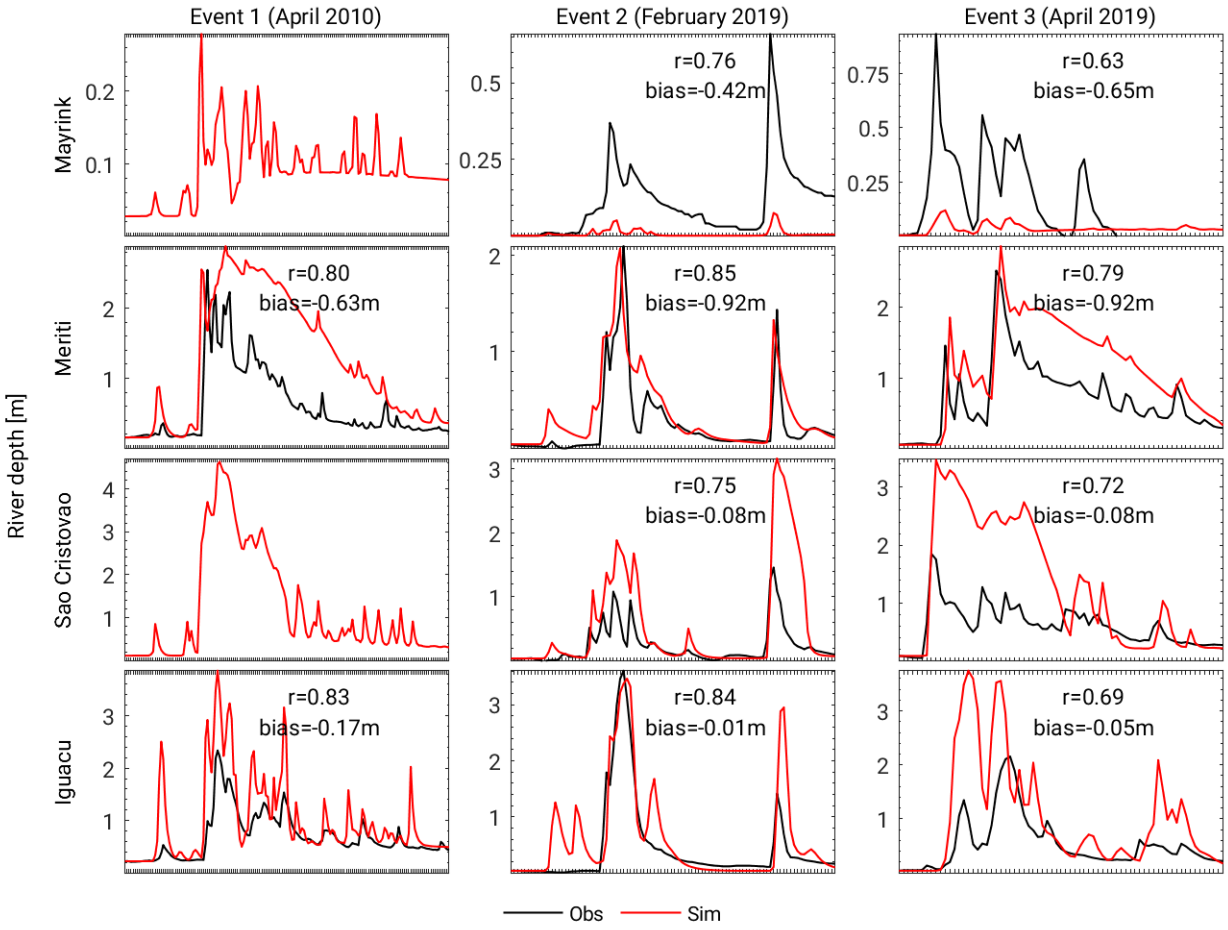

811

812 **Figure 4.** Evaluation of simulated river depth [m] at four gauges within the model domain. Bias
813 correction and correlation r are provided in panels where observations are available. Biases are
814 computed as the difference between observed and simulated depths at the first time step of each
815 event. Observations during Event 1 are not available at Mayrink and São Cristovão. Simulations
816 are derived from the *optimal* urban drainage experiment.

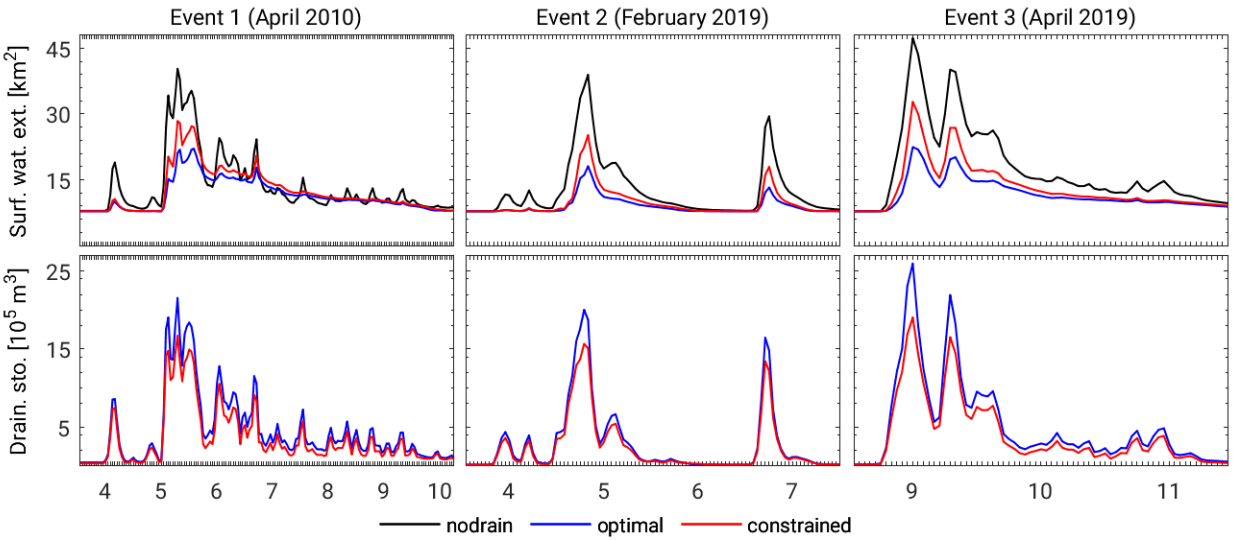

Figure 5. Impact of the urban drainage scheme on the simulation of three extreme events over urban areas in Rio de Janeiro. Top: hourly surface water extend. Bottom: hourly underground drainage water storage. Both are derived from three experiments, one neglecting (*nodrain*), and two considering (*optimal* and *constrained*) urban drainage parameterizations.

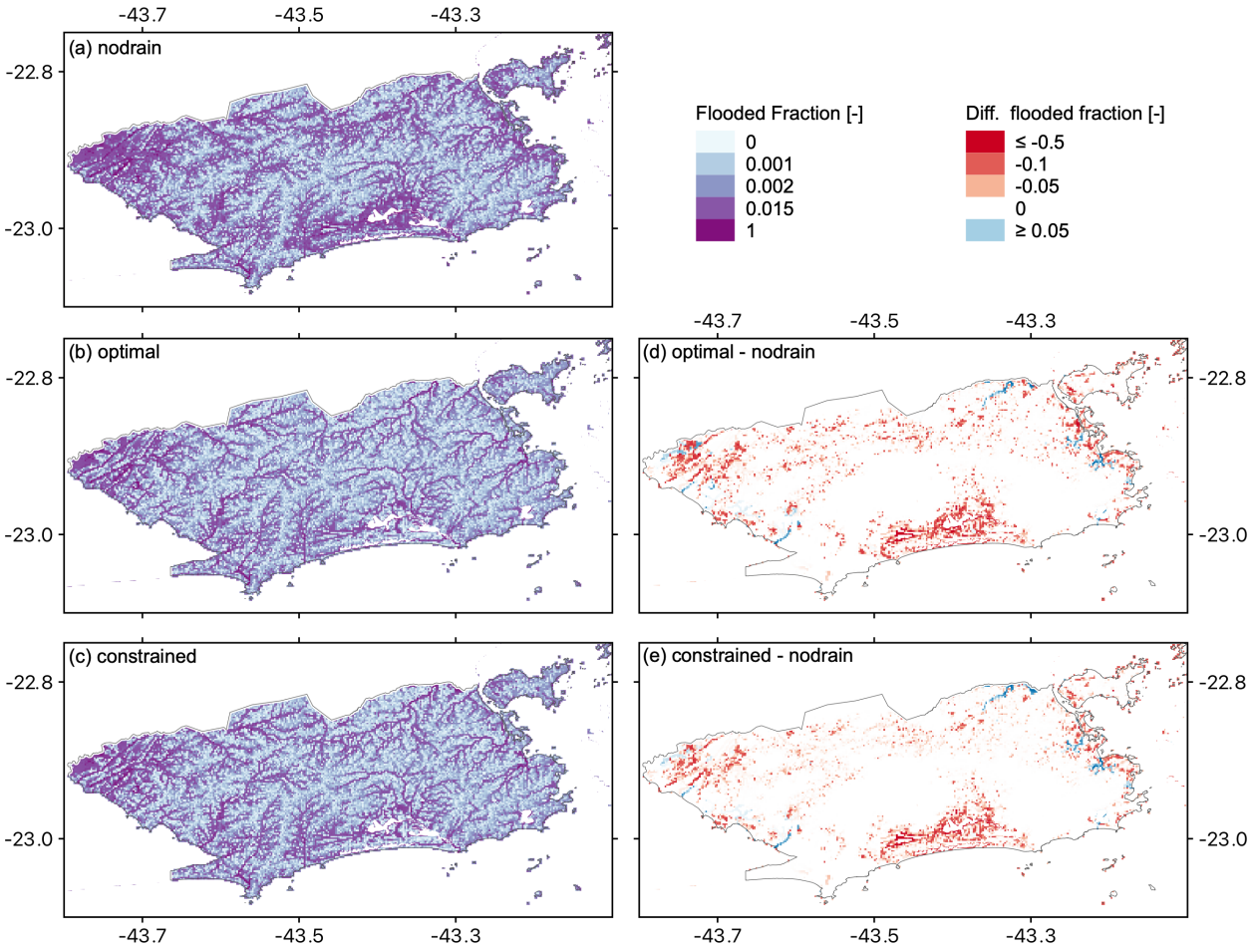

822

823 **Figure 6.** Flood fraction maps at the peak hour of Event 1 (00:00 – 6 April 2010 GMT). Values
824 are defined by the fraction of the grid surface that is covered with water, varying from zero to 1.
825 Maps are shown for each experiment in the left panels (a), (b) and (c), and differences between
826 the representation of an urban drainage system (i.e., *optimal* and *constrained*) and its absence
827 (i.e., *nodrain*) are shown in the righ panels (d) and (e). Peak hours are derived from flooding
828 time series shown in Fig. 5 using the *nodrain* experiment as baseline.

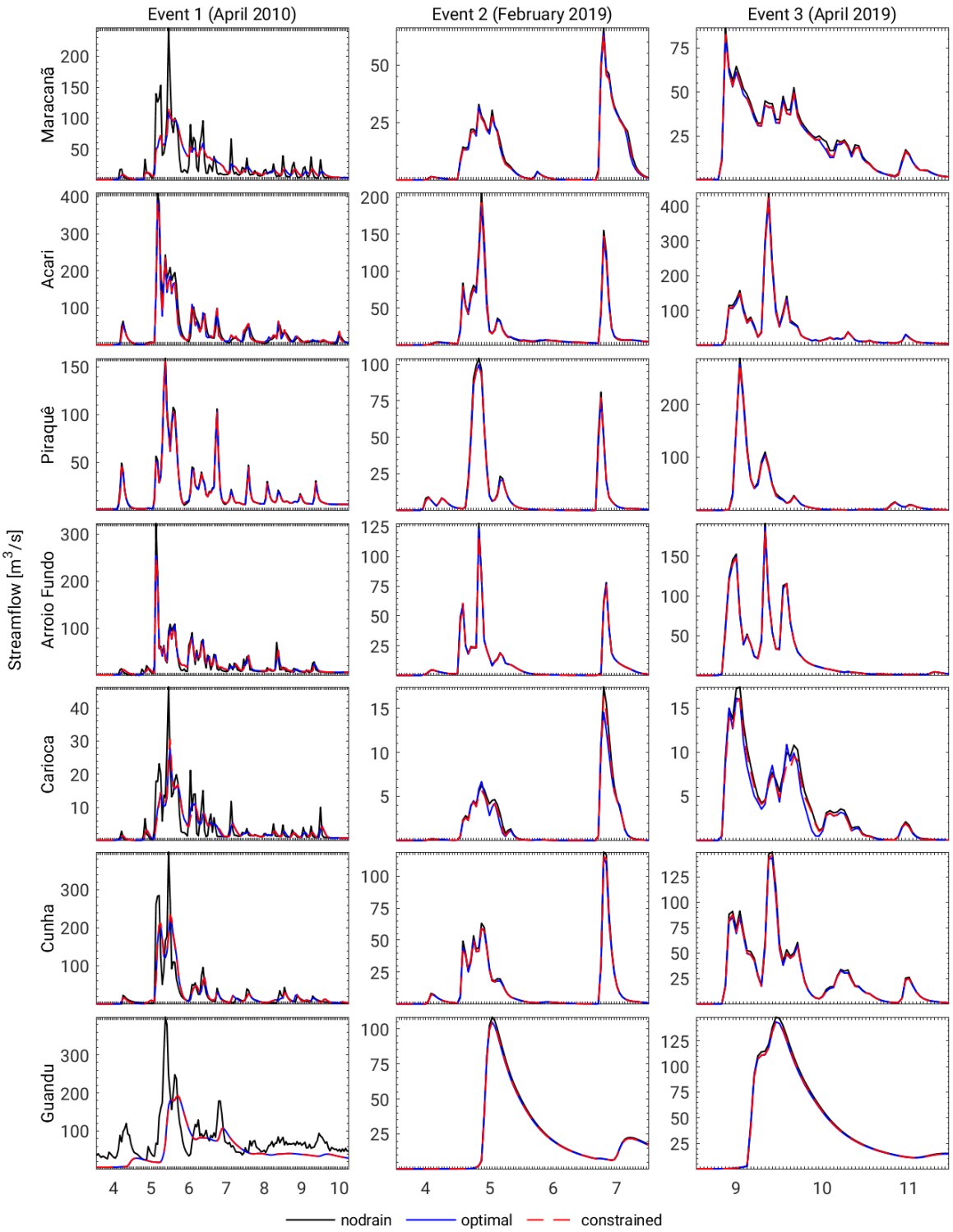

829

830 **Figure 7.** Simulated streamflow [m^3/s] at selected locations derived from three experiments.
831 Abscissa values represents days of the month. Note that ordinate magnitudes vary from panel to
832 panel.

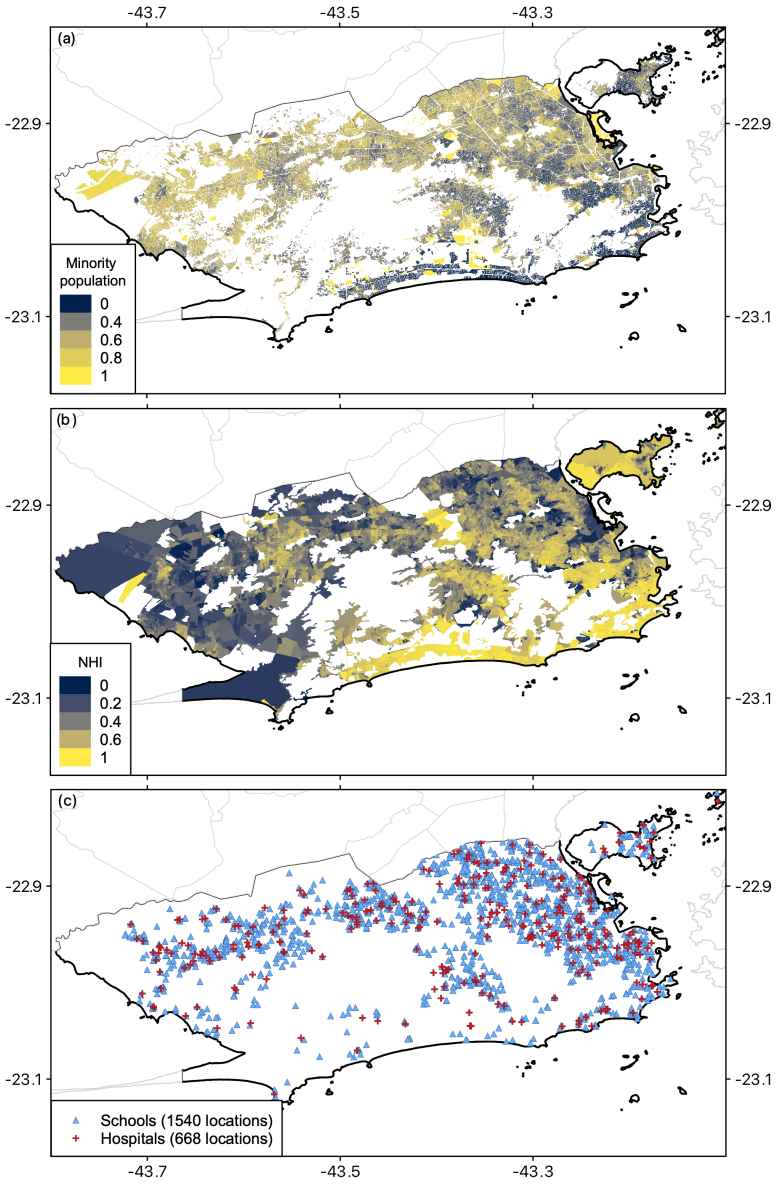

Figure 8. (a) minority population density, varying from zero to 1 (i.e., 100%), (b) normalized household income (NHI) index across Rio de Janeiro, varying from zero (lowest incomes) to 1 (highest incomes), and (c) spatial distribution of schools and hospitals. Minority population is defined as non-white Brazilians (i.e., brown, African, Asian and native Brazilians).

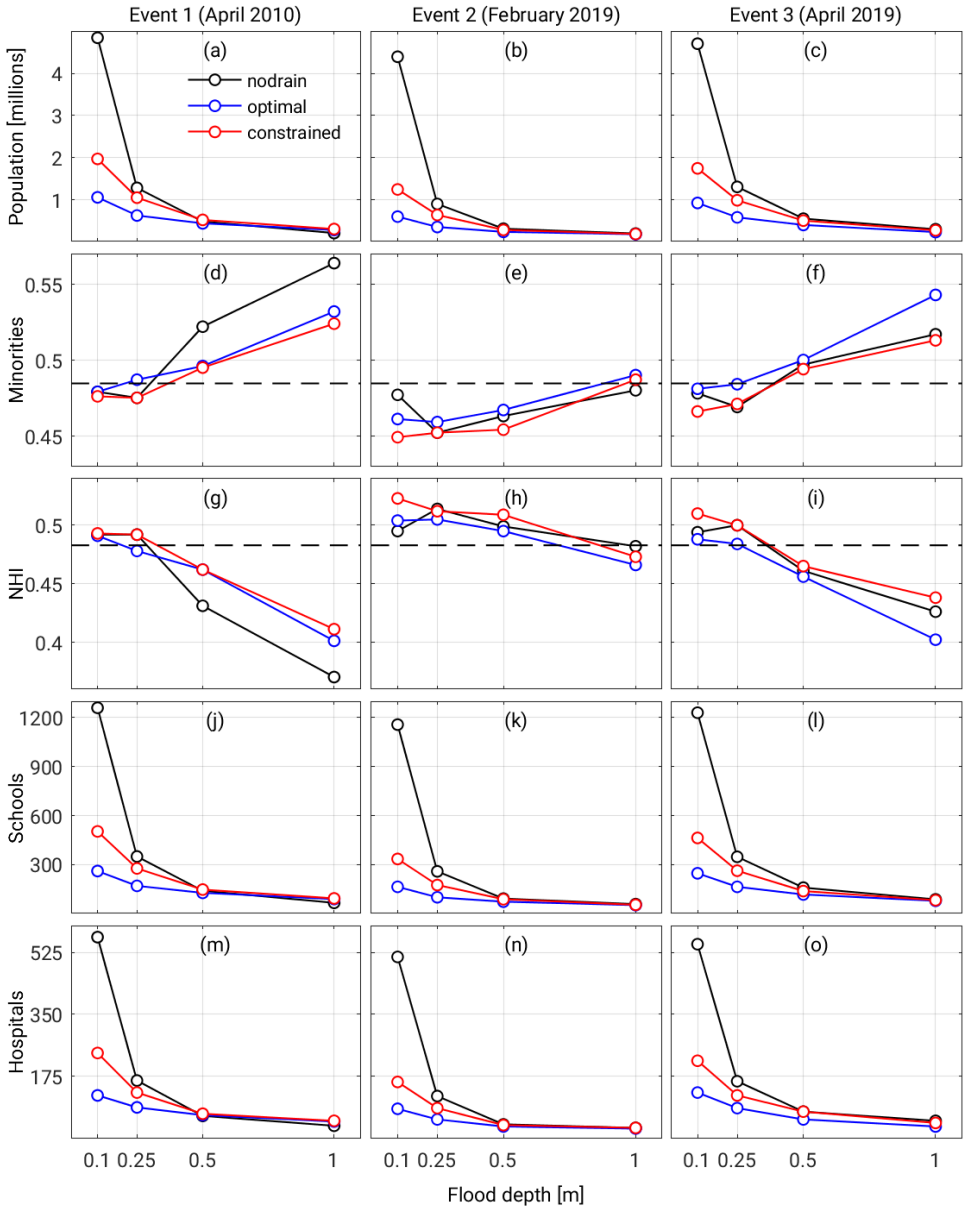

838

839 **Figure 9.** Flood exposure in terms of population count, minorities, normalized household income
840 (NHI), schools, and hospitals as a function of flood depth thresholds (i.e., ≥0.1m, ≥0.25m, ≥0.5m
841 and ≥1m). Flood depths are derived from model experiments (*nodrain*, *optimal* and *constrained*)
842 during selected extreme events. Minorities are defined as fractions of the total population
843 exposed to flooding. Black ticked lines in minorities and NHI panels represent the citywide
844 averaged values.

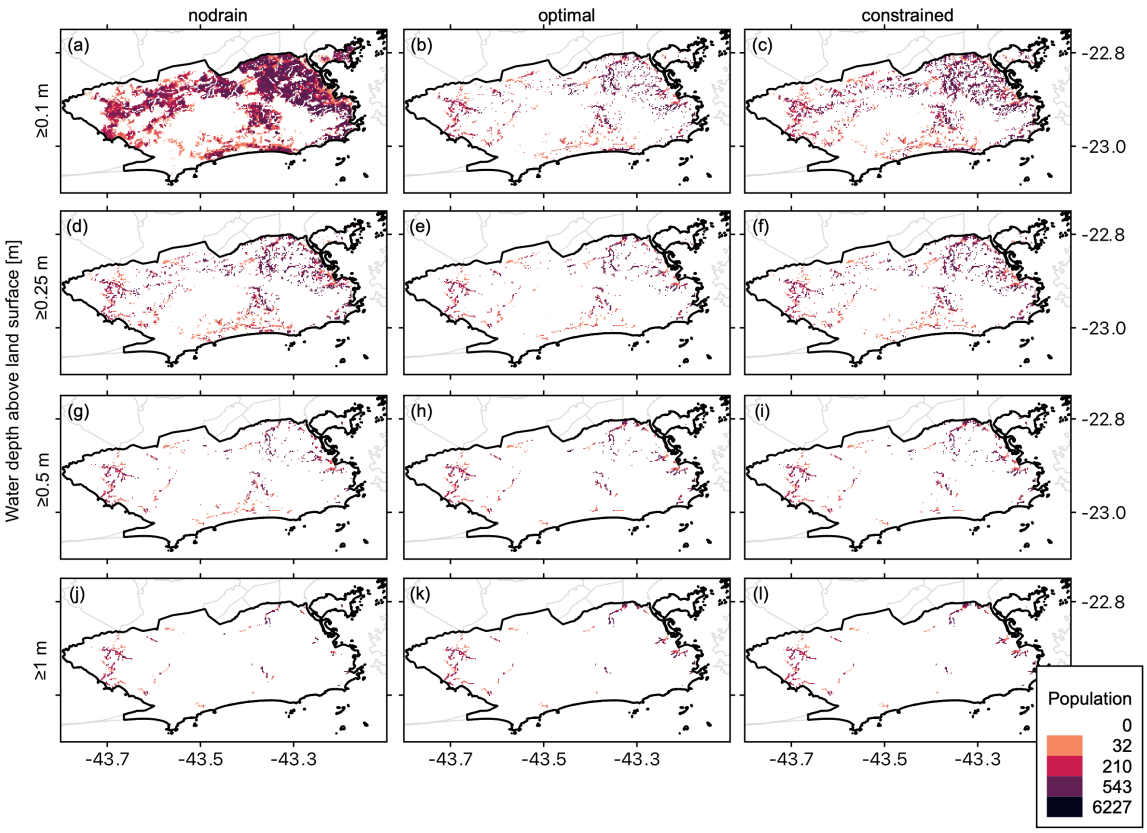

845

846 **Figure 10.** Spatial distribution of the population exposed to flooding at different thresholds of
847 water depth above the ground elevation (i.e., ≥0.1m, ≥0.25m, ≥0.5m and ≥1m) during Event 1
848 (April 2010) derived from experiments *nodrain*, *optimal* and *constrained*.

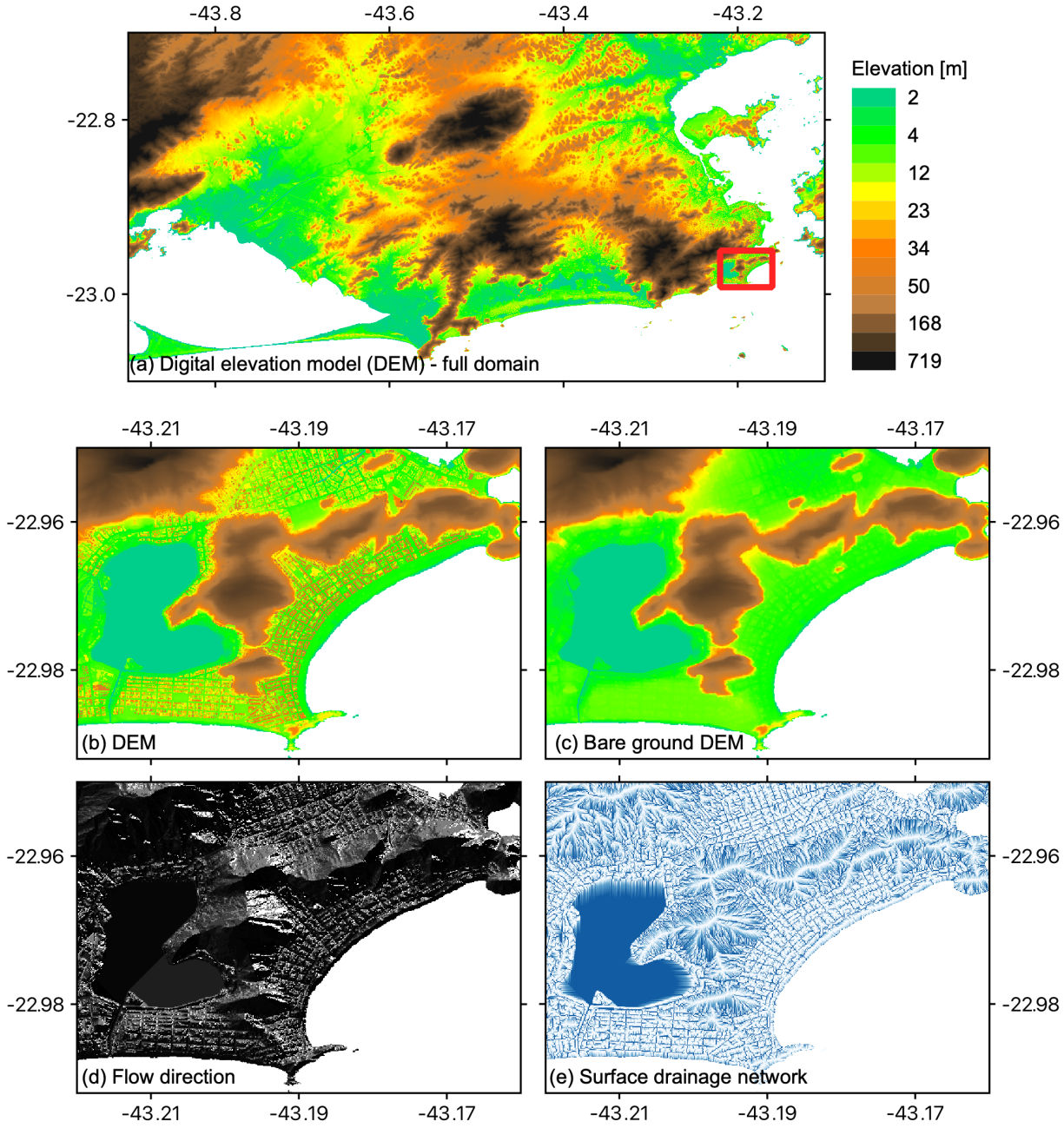

Figure A1. High-resolution digital elevation model (DEM) processing. (a) Lidar-based and MERIT DEM composite, Lidar-based (b) built-area DEM, (c) bare ground DEM, (d) flow directions and (e) surface drainage network.

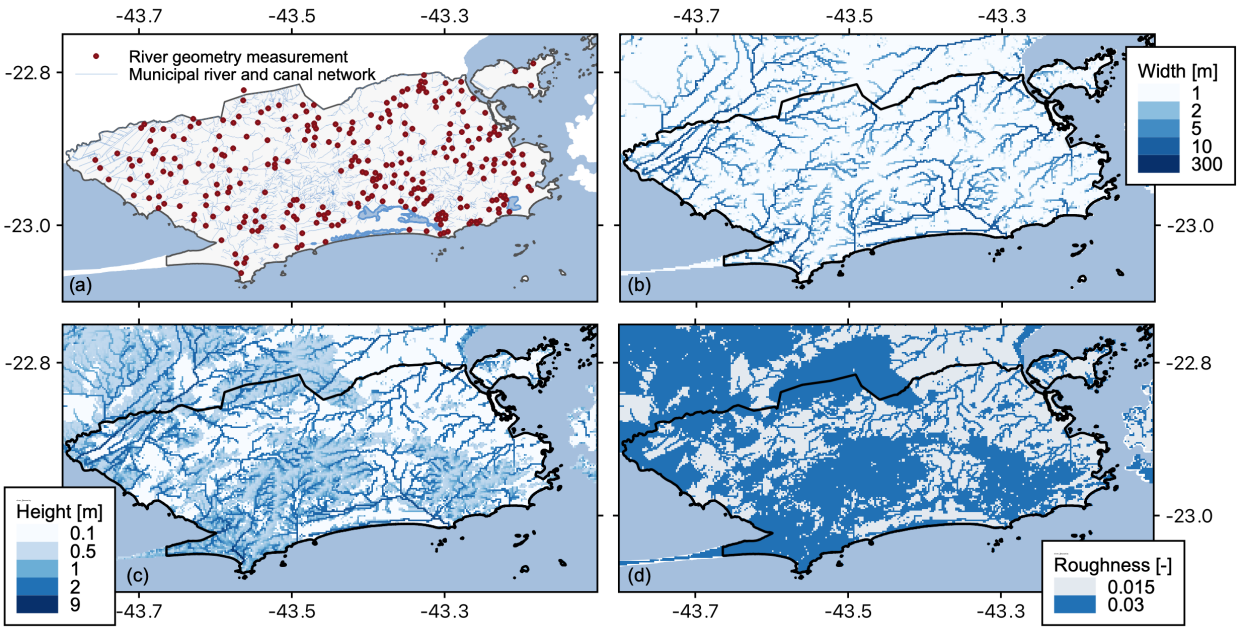

855

856 **Figure A2.** River geometry and roughness mapping. (a) 294 locations with available river width
857 and/or depth measurements, and 0.002-degree river (b) width, (c) depth, and (d) roughness.

858

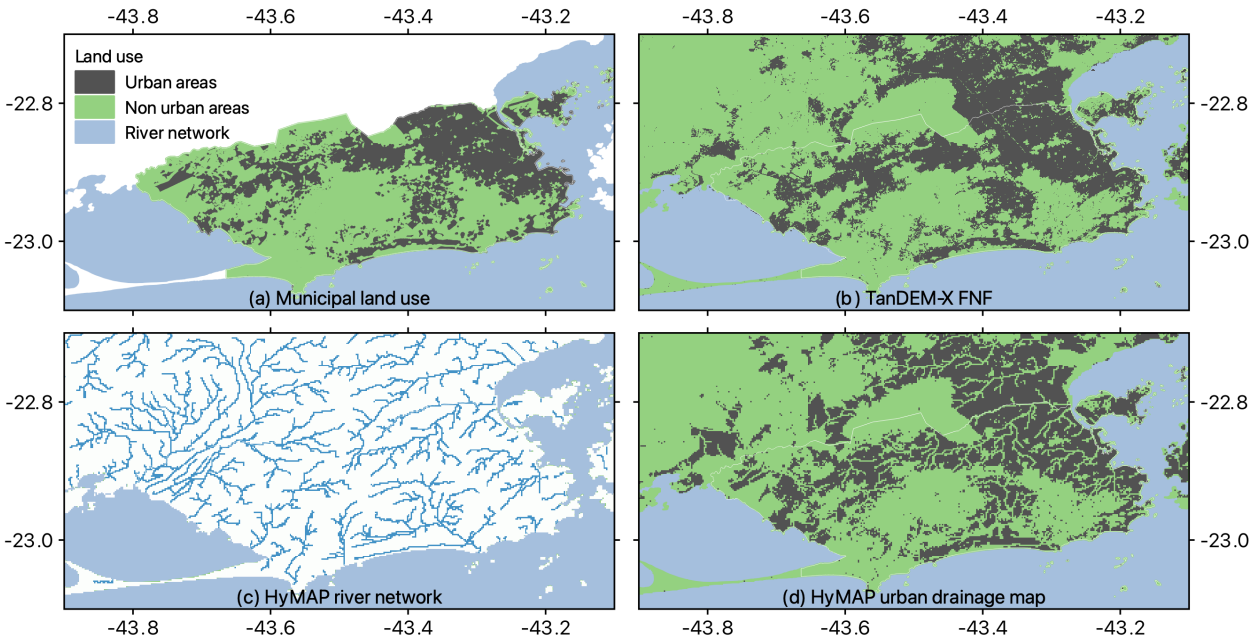

859

860 **Figure A3.** Urban drainage map generation. (a) vector-based map of municipal urban areas, (b)
861 TanDEM-X FNF-based urban areas, (c) HyMAP river network at 1.5km^2 drainage area threshold,
862 and (d) final ~200-meter resolution urban drainage map used in HyMAP.